

RapA opens the RNA polymerase clamp to disrupt post-termination complexes and prevent cytotoxic R-loop formation

Received: 18 January 2024

Accepted: 7 November 2024

Published online: 08 January 2025

 Check for updates

Joshua J. Brewer^{1,2}, Koe Inlow³, Rachel A. Mooney⁴, Barbara Bosch², Paul Dominic B. Olinares⁵, Leandro Pimentel Marcelino^{1,6}, Brian T. Chait⁵, Robert Landick^{4,7}, Jeff Gelles³, Elizabeth A. Campbell² & Seth A. Darst¹✉

Following transcript release during intrinsic termination, *Escherichia coli* RNA polymerase (RNAP) often remains associated with DNA in a post-termination complex (PTC). RNAPs in PTCs are removed from the DNA by the SWI2/SNF2 adenosine triphosphatase (ATPase) RapA. Here we determined PTC structures on negatively supercoiled DNA and with RapA engaged to dislodge the PTC. We found that core RNAP in the PTC can unwind DNA and initiate RNA synthesis but is prone to producing R-loops. Nucleotide binding to RapA triggers a conformational change that opens the RNAP clamp, allowing DNA in the RNAP cleft to reanneal and dissociate. We show that RapA helps to control cytotoxic R-loop formation in vivo, likely by disrupting PTCs. We suggest that analogous ATPases acting on PTCs to suppress transcriptional noise and R-loop formation may be widespread. These results hold importance for the bacterial transcription cycle and highlight a role for RapA in maintaining genome stability.

RNA polymerase (RNAP) is the central enzyme of transcription across all domains of life. In the canonical bacterial transcription cycle, the catalytic core RNAP (E; subunit composition $\alpha_2\beta\beta'\omega$) combines with a promoter-specificity σ factor to form the holoenzyme (E σ^{70}) capable of initiating transcription from specific promoter sequences¹. Once transcription initiates and the RNAP becomes committed to elongating the nascent RNA chain, the σ subunit generally releases (although not always)² and core RNAP completes the elongation and termination phases of the transcription cycle. Although the elongation phase is highly processive, during intrinsic termination, the completed RNA transcript is rapidly released from the complex³, followed in the canonical scheme by release of RNAP from the DNA template.

Recent single-molecule investigations have shown that the canonical bacterial transcription cycle must be reevaluated^{4,5}. In these studies, core RNAP was observed to remain associated with the template DNA after RNA transcript release at intrinsic terminators in a post-termination complex (PTC) in vitro. The RNAP in PTCs can diffuse in both directions on the DNA by sliding or hopping and can flip 180° on the DNA^{4–6}. The diffusing PTCs can sometimes initiate transcription in a promoter-dependent manner after reassociating with σ from solution, consistent with in vivo results⁴. Available data indicate that complexes with the same properties as PTCs can be reconstituted by incubating core RNAP directly with DNA (reconstituted (r)PTCs)^{4,7,8}.

The Sw2/Snf2 adenosine triphosphatase (ATPase) RapA is widespread throughout bacteria and is expressed in equal abundance to

¹Laboratory of Molecular Biophysics, The Rockefeller University, New York, NY, USA. ²Laboratory of Molecular Pathogenesis, The Rockefeller University, New York, NY, USA. ³Department of Biochemistry, Brandeis University, Waltham, MA, USA. ⁴Department of Biochemistry, University of Wisconsin-Madison, Madison, WI, USA. ⁵Laboratory of Mass Spectrometry and Gaseous Ion Chemistry, The Rockefeller University, New York, NY, USA. ⁶Tri-Institutional Program in Chemical Biology, The Rockefeller University, New York, NY, USA. ⁷Department of Bacteriology, University of Wisconsin-Madison, Madison, WI, USA. ✉e-mail: darst@rockefeller.edu

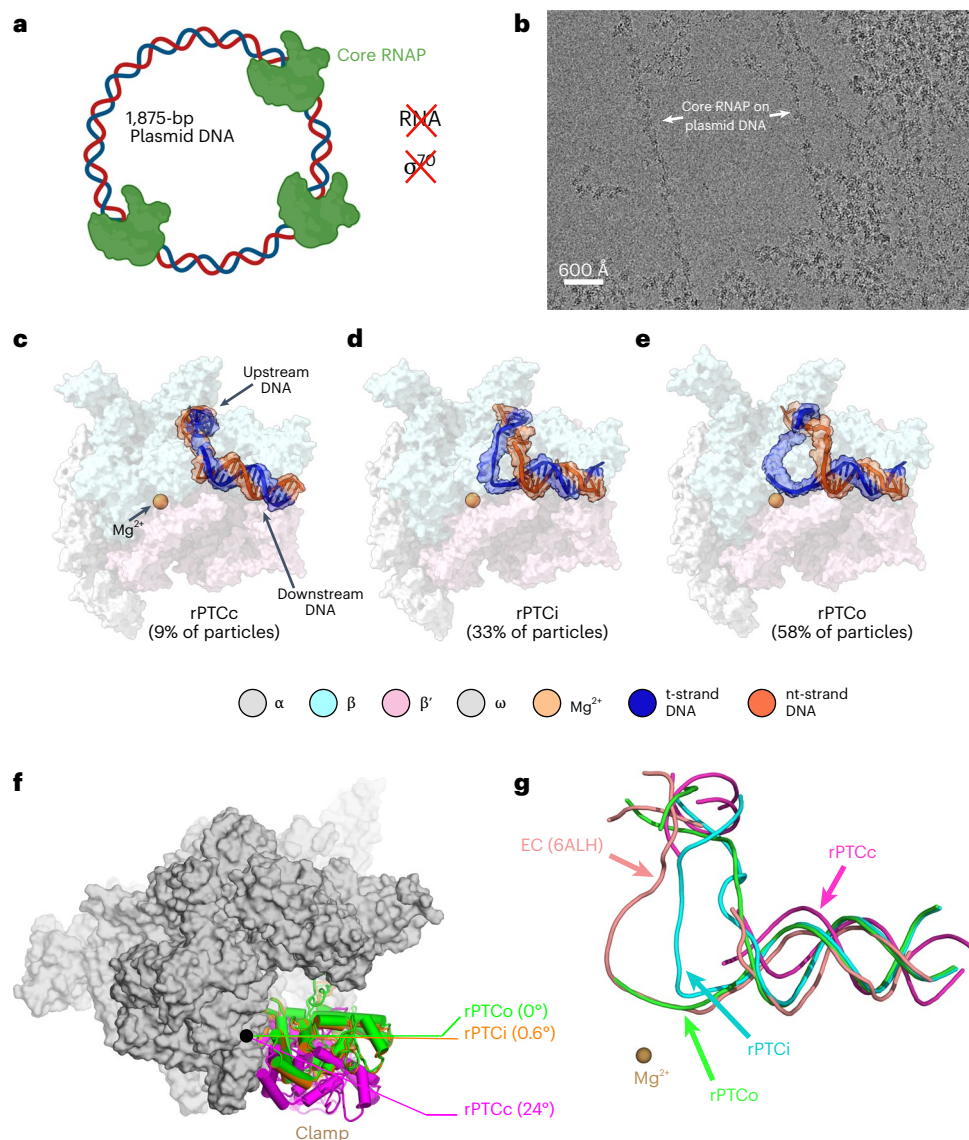


Fig. 1 | rPTCs unwind negatively supercoiled DNA. **a**, Schematic illustrating the experimental setup. *E. coli* core RNAP (green) was incubated with circular, negatively supercoiled plasmid DNA in the absence of RNA, NTPs and σ^{70} . Created with BioRender.com. **b**, Representative micrograph illustrating core RNAP molecules associated with DNA (5,043 micrographs were collected; Extended Data Fig. 1). **c–e**, Structures of rPTCc (**c**), rPTCi (**d**) and rPTCo (**e**) determined by cryo-EM. The core RNAP is shown as a transparent molecular surface, revealing the DNA and active-site Mg^{2+} in the RNAP active-site cleft. The DNA is shown in cartoon format along with transparent cryo-EM difference density. **f**, RNAP clamp conformations for the rPTC structures. The rPTCo structure was used as

a reference to superimpose rPTCc and rPTCi using the α -carbon atoms of the RNAP structural core, revealing a common RNAP structure (shown as a gray molecular surface) but with clamp conformational changes characterized as rigid-body rotations about a rotation axis perpendicular to the page (denoted by the black dot). The clamp modules are shown as backbone cartoons with cylindrical helices. The angles of clamp opening are shown relative to rPTCo (0°). **g**, Superposed DNAs from rPTCc (magenta), rPTCi (cyan), rPTCo (green) and an active EC (orange; PDB 6ALH (ref. 71)). The RNAP active-site Mg^{2+} is shown as a brown sphere.

σ^{70} in *E. coli*^{9,10}. RapA binds to core RNAP ($K_d \approx 5\text{--}10$ nM) but not $E\sigma^{70}$ (refs. 9,11). Binding of RapA to RNAP strongly stimulates RapA ATPase activity but nucleic acids neither bind strongly to RapA nor stimulate its ATPase activity^{7,9–11}. While *rapA*-null mutants do not display a clear in vivo phenotype in rich medium, stresses such as osmotic shock, exposure to sodium deoxycholate or salt stress produce a protracted recovery phase in *rapA* knockout (KO) strains^{12,13}. Additionally, *rapA* deletion diminishes antibiotic resistance in biofilms¹⁴. Lastly, in *Vibrio cholerae*, deletion of the *rapA* homolog produces a >1,000-fold decrease in colonization proficiency when cells attempt to engage the acid-tolerance response, which is important for virulence¹⁵.

Many cellular functions have been proposed for RapA^{16–21}. In in vitro transcription reactions, RapA strongly stimulates

multiround transcript production, suggesting that it acts following transcription termination^{12,16,22–24}. A recent single-molecule analysis defined the molecular target for RapA in the transcription cycle as the PTC. RapA forms a transient RapA–PTC complex that rapidly (within seconds) resolves upon ATP hydrolysis, releasing RapA and the RNAP from the DNA⁷. Although several structural studies have provided insights into the interactions between RapA and core RNAP or the RNAP elongation complex (EC)^{18,20–22}, the structural mechanism for RapA function remains elusive in part because a structure of RapA with its true molecular target, the PTC, has not been determined.

Here, we structurally and biochemically characterize *E. coli* rPTCs. We find that core RNAP can associate with negatively supercoiled DNA, is capable of generating a transcription-competent transcription

bubble de novo and can initiate RNA synthesis at physiological nucleotide concentrations, all in the absence of a σ factor. We also used a nonhydrolyzable ATP analog, ADP-AIF₃ (ref. 25), to trap RapA associated with its functional target, the rPTC. A cryo-electron microscopy (cryo-EM) structure of RapA(ADP-AIF₃)-rPTC reveals that RapA acts to impart a large conformational change in the RNAP that promotes release from the DNA. We find that rPTC-mediated σ -independent transcription generates R-loops, potentially contributing to mutagenesis and posing a threat to genome stability in vivo²⁶; however, RapA has a role in vivo in controlling R-loop formation. These findings have important implications for the canonical bacterial transcription cycle and the role of PTCs and RapA in antisense and/or pervasive transcription and genome stability²⁷.

Core RNAP forms a transcription bubble

For the structural analysis of rPTCs, we sought to eliminate the one-dimensional diffusion of the RNAP off the end of the DNA⁴ and the binding of RNAP to duplex DNA ends²⁸. We, therefore, assembled rPTCs by combining *E. coli* core RNAP with a negatively supercoiled circular DNA template, incubated briefly at 37 °C and then prepared grids for cryo-EM analysis (Fig. 1a). Visual inspection of the micrographs revealed RNAP molecules associated with DNA, including segments of extended DNA decorated with chains of RNAP molecules like beads on a string (Fig. 1b). In our processing of the micrographs, we were unable to identify particles without DNA bound in the RNAP cleft (Extended Data Fig. 1). Steps of maximum-likelihood classification²⁹ revealed three distinct conformational classes (Fig. 1c–f, Table 1 and Extended Data Figs. 1 and 2). The cryo-EM density for the DNA in each of the classes was poorly resolved compared to the RNAP density, consistent with the expected local heterogeneity in the DNA because of the nonspecific association of rPTCs and lateral diffusion. The DNA was modeled with the aid of previously determined DNA–RNAP complexes³⁰ and features of the DNA were conservatively interpreted.

In the closed-DNA rPTC (rPTCc, ~9% of the particle population; 4.7-Å nominal resolution; Fig. 1c and Extended Data Figs. 1 and 2a–c), the RNAP clamp^{31,32} was notably wide open (24° open compared to a 0° reference) (Fig. 1f). The RNAP cleft was occupied with severely kinked (~90°) but mostly duplex (closed) DNA (Fig. 1c). The vicinity of the DNA kink was poorly resolved and potentially a site of bubble nucleation, with the conserved switch 2 (Sw2) and fork loop 2 (FL2) RNAP structural elements³² proximal to the kink (Extended Data Fig. 3a). The RNAP β' rudder was well resolved, situated in the major groove of the upstream double-stranded DNA (Extended Data Fig. 3a).

In the intermediate-bubble rPTC (rPTCi; 33% of the particle population; 3.8-Å nominal resolution; Fig. 1d and Extended Data Figs. 1 and 2d–f), the RNAP clamp was relatively closed (0.6°) (Fig. 1f). The RNAP cleft was occupied by DNA with a clear melted bubble of ~5 nt enclosed completely within the cleft (Fig. 1d). The single-stranded nontemplate strand (nt-strand) DNA was relatively well resolved but the template-strand (t-strand) was dynamic, poorly resolved and not near the active site (Fig. 1g and Extended Data Fig. 3b).

The downstream fork junction of the rPTCi bubble appears to be stabilized by the insertion of Sw2 and FL2 elements between the melted strands at the downstream edge of the bubble (Extended Data Fig. 3b). The stabilized downstream fork junction observed together with the Sw2–FL2 insertion is consistent with prior biochemical findings implicating Sw2 in DNA melting, initiating-nucleotide binding and promoter escape, along with EC stability^{33,34}. The β' rudder, previously implicated in EC and RPo stability³⁵, was disordered because of a clash between the rudder and the duplex DNA immediately upstream of the growing bubble (Extended Data Fig. 3b).

In the open-bubble rPTC (rPTCo, 58% of the particle population; 3.6-Å nominal resolution; Fig. 1e and Extended Data Figs. 1 and 2g–i), the RNAP clamp was closed on the DNA (Fig. 1f). The RNAP cleft was occupied by DNA with a more extensive bubble of ~7–8 nt (the upstream edge

of the bubble was poorly resolved), which propagated in the upstream direction compared to the smaller bubble in rPTCi (Fig. 1d,e). As in rPTCi, the single-stranded nt-strand DNA was relatively well resolved while the t-strand was dynamic and poorly resolved but occupied positions near the RNAP active-site Mg²⁺, similar to a bona fide EC (Fig. 1g).

As in rPTCi, the Sw2 and FL2 elements of rPTCo were inserted between the melted stands at the downstream fork of the transcription bubble (Extended Data Fig. 3c). The β' rudder was resolved and fully inserted between the two melted strands, likely stabilizing the upstream edge of the bubble (Extended Data Fig. 3c).

Rotation of a swivel module is associated with paused ECs and appears to inhibit RNAP motions required to complete nucleoside triphosphate (NTP) binding, catalysis and translocation^{30,36–38}. Compared to an unswiveled reference structure (Protein Data Bank (PDB) 8EG8 (ref. 30)), both rPTCi and rPTCo were substantially swiveled (4.4° and 4.0°, respectively) (Extended Data Fig. 4).

Cryo-EM structure of RapA(ADP-AIF₃)-rPTC

Recent work identified PTCs as the target of the SWI2/SNF2 ATPase RNAP recycling factor RapA⁷. Inlow et al.⁷ used single-molecule analyses to identify two kinetically distinct RapA–rPTC assemblies formed during ATP-dependent RNAP recycling (denoted RapA–PTC and RapA[†]–PTC) and proposed a kinetic scheme in which these assemblies are intermediates in the disruption of PTCs by RapA (Extended Data Fig. 5a). Initial RapA association with PTCs was independent of nucleotide in solution, consistent with the first intermediate, RapA–PTC, containing apo RapA (Extended Data Fig. 5a). Cryo-EM structures of apo RapA engaged with core RNAP (PDB 7MKQ (ref. 18)) and with ECs (PDB 7MKN (ref. 18) and PDB 7M8E (ref. 21)) all yielded closed-clamp RNAP structures bound to apo RapA in a nearly identical pose, suggesting that the configuration of the complex of apo RapA with RNAP is independent of the nucleic acid binding status of the RNAP. We, therefore, propose that the apo RapA–RNAP and apo RapA–EC structures represent good models for the structure of the first RapA–PTC intermediate.

The second kinetically distinct intermediate, RapA[†]–PTC, leads to PTC disruption at a rate that is strongly dependent on nucleotide in solution⁷. In the presence of ATP, PTC disruption by RapA was at least 150-fold faster than when ATP was absent or when a nonhydrolyzable ATP analog was present. In the presence of the analog, RapA[†]–PTC was >20-fold more stable than the first intermediate and more than half of the assemblies exhibited a characteristic lifetime close to 5 min (ref. 7), a time scale compatible with cryo-EM grid preparation. Therefore, we generated rPTCs on negatively supercoiled circular DNA (Fig. 1a), subsequently introduced RapA complexed with the nonhydrolyzable ATP analog ADP-AIF₃ (ref. 25) and analyzed the resulting complexes using single-particle cryo-EM (Extended Data Fig. 5b). The results revealed a RapA(ADP-AIF₃)-PTC structure (3.6-Å nominal resolution; Fig. 2a, Extended Data Fig. 5b,c and Table 1) with new characteristics compared to previously described RapA–RNAP or RapA–EC complexes^{18,21}, which we equated with RapA[†]–PTC (Extended Data Fig. 5a). These new properties include (1) the conformation of RapA; (2) the overall disposition of RapA with respect to the RNAP; and (3) the conformation of RNAP and the associated DNA. Cryo-EM density in the RNAP cleft of RapA[†]–PTC was consistent with kinked duplex DNA (Fig. 2a), very similar to the DNA occupying the rPTCc RNAP cleft (Fig. 1c). The cryo-EM density for RapA was relatively poorly resolved compared to the RNAP (Extended Data Fig. 5c), presumably because of conformational heterogeneity that could not be resolved by classification. The molecular model for RapA was initially constructed by rigid-body fitting of previously determined RapA domains^{21,22}. Modeling of the nucleotide bound in the RapA active site (Fig. 2b) was guided by the structure of a RecA ATPase homolog bound to a nonhydrolyzable ATP analog (chromodomain–ATPase portion of yeast Chd1 chromatin remodeler; PDB 3MWY (ref. 39)).

Table 1 | Cryo-EM data collection, refinement and validation statistics for RapA[†]-PTC and rPTC classes

Dataset	rPTC			RapA [†] -PTC
Data collection and processing				
Microscope	FEI Titan Krios			FEI Titan Krios
Voltage (kV)	300			300
Detector	Gatan K3			Gatan K3
Electron exposure (e ⁻ per Å ²)	55.9			52.1
Defocus range (μm)	-0.25 to -4.2			-0.8 to -2.5
Data collection mode	Counting mode			Counting mode
Pixel size (Å)	1.076			1.076
Symmetry imposed	C1			C1
Initial particle images (no.)	1,261,036			3,560,985
Refinement				
Structure	rPTCc	rPTCi	rPTCo	RapA [†] -PTC
EM Data Bank	EMD-40930	EMD-40931	EMD-40922	EMD-40943
PDB	8T00	8T02	8SZW	8T0L
Final particle images (no.)	13,101	49,701	86,865	100,010
Map resolution (Å) FSC threshold=0.143	4.7	3.8	3.6	3.6
Map resolution range (Å)	3.4–7.8	2.4–6.9	2.8–6.9	2.8–7.2
Initial model used (PDB code)	6ALH	6ALH	6ALH	Ab initio using screening dataset
Map sharpening B factor (Å ²)	-126.0	-108.9	-114.5	-117.5
Model composition				
Nonhydrogen atoms	50,247	51,102	51,717	65,326
Protein residues	3,093	3,146	3,183	4,152
Nucleic acid residues (DNA)	52	51	52	-
Ligands	2 Zn ²⁺ , 1 Mg ²⁺ , 1 ADP-AlF ₃			
B factors (Å²)				
Protein	289.6	109.2	69.94	166.2
Nucleic acid	515.0	247.9	134.2	-
Ligands	382.0	139.8	83.67	233.2
Root-mean-square deviations				
Bond lengths (Å)	0.003	0.004	0.003	0.005
Bond angles (°)	0.662	0.643	0.63	0.668
Validation				
MolProbity score	1.82	1.99	1.83	2.62
Clashscore	7.07	9.67	7.68	9.74
Poor rotamers (%)	0	0.22	0.22	5.59
Ramachandran plot				
Favored (%)	93.49	92.06	93.93	90.2
Allowed (%)	6.48	7.91	5.97	9.68
Disallowed (%)	0.03	0.03	0.09	0.12

ADP-AlF₃ triggers global conformational changes in RapA

The cryo-EM density of RapA[†]-PTC clearly showed ADP-AlF₃ occupying the RapA nucleotide-binding site between the 1A and 2 (RecA) domains (Fig. 2b). The RapA domains discussed herein are defined in Supplementary Table 1. As expected for a RecA-type ATPase⁴⁰, occupancy of the nucleotide-binding site gave rise to a large change in the orientation of the RecA ATPase domains with respect to each other (RapA domains 1A and 2; Fig. 2b) compared to apo RapA structures^{18,21}, corresponding to a 33° rotation of domain 2 toward domain 1A (Fig. 2b). This large conformational change induced by ADP-AlF₃ binding triggered a complex

series of allosteric conformational changes in the other RapA domains (with respect to the reference domain 1A; Fig. 2b and Supplementary Video 1), most notably resulting in a motion of the RapA N-terminal domain (NTD) corresponding to a 51° rotation and a 27-Å translation of the domain center of mass (Fig. 2b).

RapA conformational changes mechanically open the RNAP clamp

Comparing apo RapA-EC (PDB 7M8E (ref. 21)) to RapA[†]-PTC, the binding of ADP-AlF₃ induced substantial conformational changes in RapA (Fig. 2b and Supplementary Video 1). These changes were accompanied

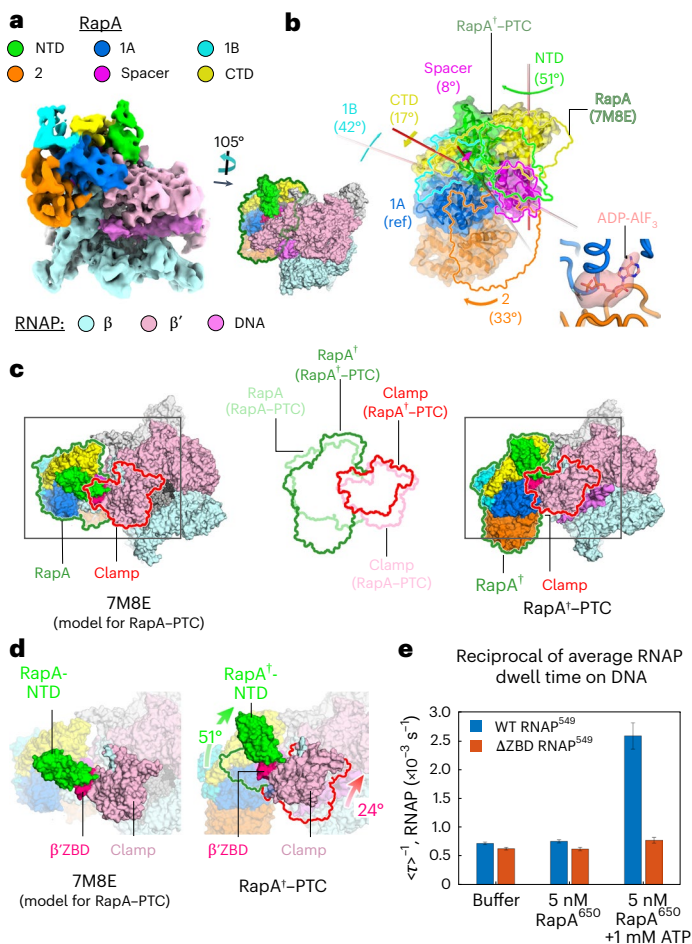


Fig. 2 | RapA opens the RNAP clamp to promote DNA dissociation. **a**, Cryo-EM map (local resolution filtered)⁷² of RapA(ADP-AIF₃)-rPTC (RapA¹-PTC). **b**, Conformational changes in RapA. Bottom left: overall view of RapA¹-PTC. The relationship between this view and the view in **a** is shown. RapA, partially obscured by RNAP, is outlined in green. Middle: RapA structures from apo RapA-PTC (PDB 7M8E)²¹ and RapA¹-PTC were superimposed using the 1A domain (Supplementary Table 1). RapA¹ is in cartoon format with transparent molecular surfaces; apo RapA domains are colored outlines. Rotations for the conformational changes of each domain (apo RapA→RapA¹) are shown. Note the large 51° rotation of the RapA NTD (green). Bottom right: zoomed-in view of the nucleotide-binding site (between the 1A and 2 domains). Modeled ADP-AIF₃ and cryo-EM difference density (transparent surface) corresponding to the bound nucleotide are shown. **c**, Overall change in architecture of apo RapA-PTC and RapA¹-PTC. Left: apo RapA-PTC shown as a molecular surface. RNAP surfaces are transparent, showing nucleic acids inside the RNAP cleft (t-strand DNA, dark gray; nt-strand DNA, light gray; RNA, red). RapA and the RNAP clamp are outlined in green and red, respectively. Right: RapA¹-PTC shown similarly with transparent RNA surfaces revealing DNA inside the cleft. Middle: superimposed outlines of RNAP clamps from apo RapA-PTC (lighter shades) and RapA¹-PTC. The entire RapA molecule rotates 65° on the RNAP surface and the clamp opens 24°. **d**, Boxed regions of **c** are magnified, highlighting the RapA NTD:β'ZBD interface. Left: apo RapA-PTC. Right: RapA¹-PTC. The green and red outlines denote positions of the RapA NTD (green) and RNAP clamp (red) from apo RapA-PTC. A 51° rotation of RapA¹ NTD results in a 24° clamp opening. **e**, Results from single-molecule fluorescence microscopy measuring effective dissociation rates (reciprocal of the average RNAP dwell time on DNA, τ^{-1}) of surface-tethered rPTCs formed with RNAP or a ΔZBD RNAP mutant by RapA plus ATP or in controls lacking RapA or ATP. Number of complexes from left to right: $n = 308, 184, 306, 122, 272$ and 130. Data are presented as the mean values \pm s.e.m. (further results in Extended Data Fig. 6c).

by a large rearrangement of RapA as a whole, corresponding to a 65° rotation of RapA relative to the RNAP (Fig. 2c and Supplementary Video 2).

Major RapA–RNAP interfaces include the RecA domains (RapA domains 1A and 2; Fig. 2b) with the RNAP β flap tip and the RapA NTD with the RNAP β' zinc-binding domain (ZBD) (Fig. 2c,d). The main anchor point for the 65° RapA rotation (with respect to the RNAP) is the RapA 1A:β flap tip interaction. The rotation of RapA about this anchor point, which is accommodated by flexibility of the β flap tip (Extended Data Fig. 6a and Supplementary Video 2), results in the large motion (51° rotation, 27-Å translation) of the RapA NTD described previously (Fig. 2b,c). The RapA NTD forms a notable interface with the β'ZBD (583-Å² interface area⁴¹); consequently, the large motion of the RapA NTD pulls the β'ZBD and associated RNAP clamp with it, resulting in a 24° opening of the RNAP clamp (Fig. 2c,d and Supplementary Video 2). The RapA spacer domain also appears to wedge itself into the now open RNAP cleft, possibly stabilizing the open-clamp conformation (Extended Data Fig. 6b).

The relatively closed clamps observed in the rPTCo and rPTCi structures were accompanied by DNA melting observed in those structures (Fig. 1d,e), whereas rPTCc, with its open clamp, contained apparently closed, duplex DNA in its RNAP cleft (Fig. 1c). Similarly, the cryo-EM density in the RNAP cleft of the open-clamp RapA¹-PTC is consistent with duplex DNA (Fig. 2a). Clamp opening in RapA¹-PTC would not only allow the DNA to anneal into a duplex but also be expected to destabilize DNA binding and promote dissociation of the DNA.

The RapA NTD pulls on the β'ZBD to open the RNAP clamp

Our model for RapA function predicts that the RapA NTD:β'ZBD interface is crucial, allowing the motion of the RapA NTD to pull on the β'ZBD and open the RNAP clamp. We tested this model by assessing the ability of RapA to disrupt PTCs generated from an RNAP derivative lacking the β'ZBD (ΔZBD RNAP). Non-supercoiled fluorescently labeled DNA circles tethered to the surface of a glass flow chamber were preincubated with either 1.5 nM RNAP or 4 nM ΔZBD RNAP, each dye-labeled with a SNAP tag fusion to the β' subunit C terminus (RNAP⁵⁴⁹ and ΔZBD RNAP⁵⁴⁹, respectively). Single-molecule total internal reflection microscopy (smTIRF) revealed individual molecules of RNAP at the locations of single DNA molecules, indicating rPTC formation. Note that a higher concentration of ΔZBD RNAP⁵⁴⁹ was required to achieve quantities of rPTCs optimal for experiments; at 1.5 nM RNAP⁵⁴⁹, we attained 40–50% DNA occupancy by RNAP, compared to ~25% occupancy with 4 nM ΔZBD RNAP⁵⁴⁹.

As previously reported⁷, replacement of the flow chamber solution with a buffer containing 1 mM ATP and a fluorescent RapA derivative (5 nM RapA⁶⁵⁰) accelerated the loss of RNAP from the surface compared to controls without RapA or without ATP (Fig. 2e and Extended Data Fig. 6c), indicating rPTC disruption. By contrast, no disruption above the control was detected with ΔZBD RNAP, highlighting the essential role of the interaction between the RapA NTD and the RNAP β'ZBD in stimulating RNAP clamp opening and subsequent dissociation of RNAP from DNA.

Core RNAP can initiate transcription

Given the DNA disposition in rPTCo and the possibility that the t-strand DNA can occupy a position near the RNAP active site similar to an active EC (Fig. 1g), we compared the transcription activity of the rPTCs to that of Eo⁷⁰ on a circular DNA plasmid template containing the strong T7A1 promoter and T7 intrinsic terminator sequence, expected to yield a specific 161-nt transcript with Eo⁷⁰ (Fig. 3a). We used relatively high NTP concentrations (500 μM each) to approximate physiological concentrations⁴²; however, note that the relatively high E concentration (0.5 μM) was chosen to drive rPTC formation and not to mimic physiological conditions, where the concentration of free E is very low⁴³. The

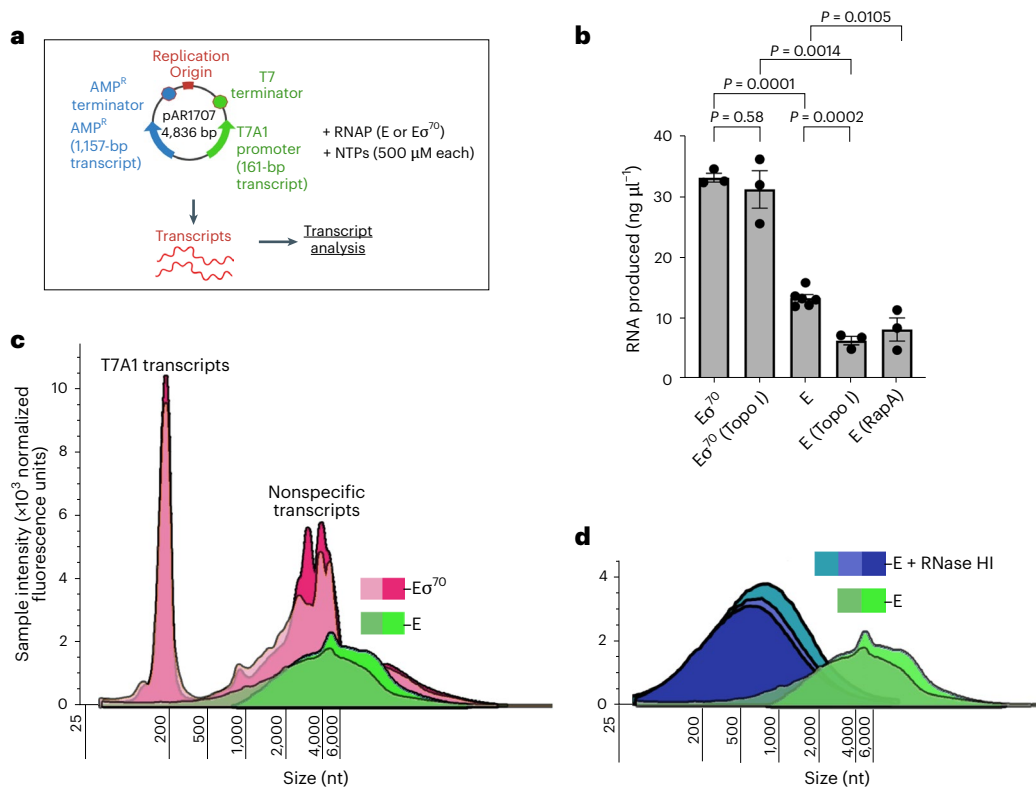


Fig. 3 | Transcription initiation by core RNAP. **a**, Schematic illustrating the experimental setup. *E. coli* core RNAP (E) or $E\sigma^{70}$ was incubated with circular, negatively supercoiled plasmid DNA (paAR1707)⁷³ in the presence of NTPs (500 μ M each) for 15 min at 37 $^{\circ}$ C. The total amount and size distribution of the resulting RNA transcripts were then analyzed. **b**, Histogram plot showing the total amount of RNA produced from each transcription reaction. The bars denote the average of three to six independent measurements (individual data points shown). Data are presented as the mean values \pm s.e.m. The

statistical significance of differences between samples was determined using unpaired, two-tailed *t*-test. **c**, Size distribution of transcripts resulting from two independent $E\sigma^{70}$ transcription reactions (red shading) and two independent core RNAP reactions (green shading). The area under the curve for each profile was normalized according to the total RNA produced. **d**, Size distribution of transcripts resulting from the core RNAP reactions (green shading) along with similar reactions treated with RNase HI (blue shades). The area under the curve for each profile was normalized according to the total RNA produced.

resulting RNA transcripts were extracted and quantified and the size distributions were analyzed.

The overall amount and size distribution of the RNA produced by core RNAP versus $E\sigma^{70}$ were clearly distinct (Fig. 3b,c), confirming the absence of notable σ^{70} contamination in our purified core RNAP. As expected, the transcription reactions with core RNAP produced less total RNA than $E\sigma^{70}$ (about threefold less; Fig. 3b). Reactions using plasmid DNA preincubated with topoisomerase I to relax supercoils showed a marked (more than twofold) decrease in core RNAP transcription, whereas $E\sigma^{70}$ transcription was unaffected; core RNAP transcription on the topoisomerase I-treated template was \sim 6-fold less than $E\sigma^{70}$ (Fig. 3b). Transcription from the T7A1 promoter has been shown to be relatively insensitive to DNA supercoiling⁴⁴. The decreased core RNAP transcription on relaxed DNA could be explained by a decrease in the overall number of PTCs or a decrease in the transcription activity of the PTCs. Because PTCs on relaxed DNA are extremely stable ($K_d < 15$ nM)⁸, we favor the hypothesis that negative supercoiling shifts the equilibrium away from transcriptionally inactive PTCc and PTCi and toward transcriptionally active PTCo (Fig. 1c–e).

The size profile of the RNA products for the $E\sigma^{70}$ reactions was dominated by the expected specific transcript of 161 nt (Fig. 3c). Additional smaller peaks were superimposed onto a broad distribution of RNAs spanning approximately 1 kb to >6 kb in length (Fig. 3c). By contrast, the core RNAP transcription products were characterized by a broad, relatively featureless distribution of RNAs over similar RNA lengths (1 kb to >6 kb; Fig. 3c), consistent with nonspecific transcription initiation by the rPTCs. We repeated the transcription reactions, comparing $E\sigma^{70}$ to E on a derivative of pAR1707, pJB2, that lacked the

strong T7A1 promoter (as well as all but one other annotated promoter; Extended Data Fig. 7). As expected, the amount and size profile of $E\sigma^{70}$ transcripts from pJB2 were substantially altered compared to pAR1707 (Extended Data Fig. 7c,d). By contrast, the amount and size profile of E transcripts from pJB2 and pAR1707 were nearly identical (Extended Data Fig. 7c,e), indicating that the presence of the strong T7A1 promoter on pAR1707 had little to no effect on transcription initiated by E. These results clearly indicate that rPTCs can nonspecifically initiate transcription, consistent with the cryo-EM structure of rPTCo that shows a complex containing a bubble with the t-strand loaded into the active site (Fig. 1e).

PTC-initiated transcription is prone to R-loop formation

We noted that the broad distribution of large RNAs (>1 kb) for both $E\sigma^{70}$ and core transcription reactions contained substantial amounts of RNA chains longer than the plasmid itself (4.836 kb). We hypothesize that nonspecific rPTC initiation generates elongating complexes with R-loops (persistent RNA–DNA hybrid) in their wake. The upstream RNA–DNA hybrid would prevent the formation of RNA secondary structure in the upstream transcript (such as terminator hairpins), causing the RNAP to ignore terminators and continuously transcribe around the circular DNA template in a rolling-circle transcription mechanism (*E. coli* RNAP can produce >7 kb transcripts from circular DNA templates in this manner)⁴⁵.

Treatment of the PTC transcription reactions with *E. coli* RNase HI, which specifically hydrolyzes the RNA phosphate backbone when the RNA is hybridized to DNA, significantly reduced the size distribution

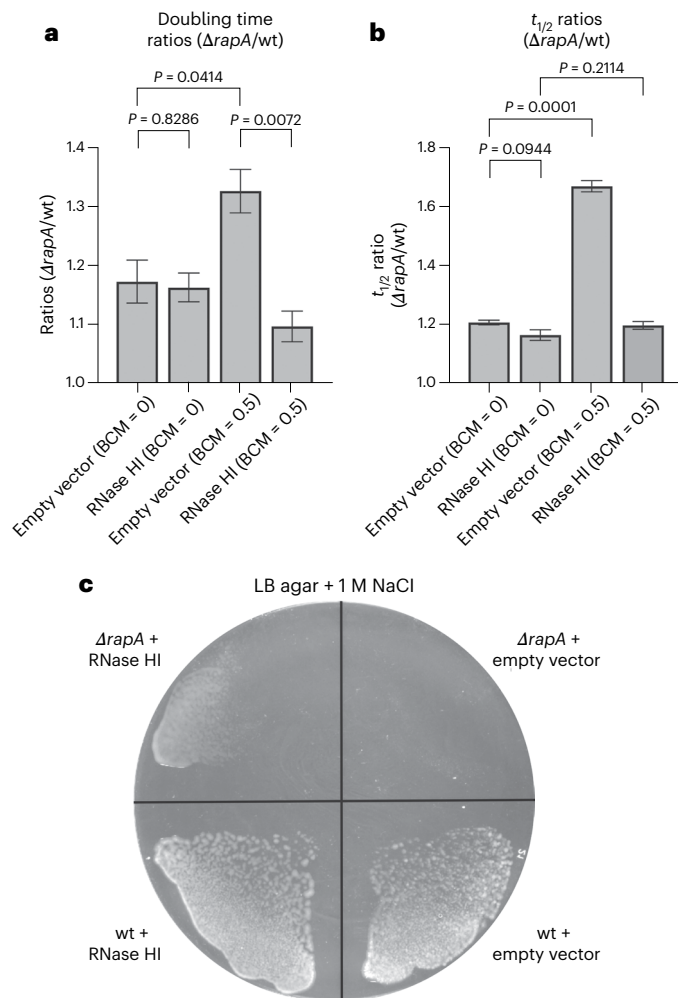


Fig. 4 | RapA suppresses cytotoxic R-loops in vivo. **a, b**, Growth parameters (doubling times (**a**) and $t_{1/2}$ (**b**)) for wt and $\Delta rapA$ *E. coli* cells carrying pBAD18 (empty vector)⁷⁴ or pBAD18*rnhA* (RNase HI)⁵¹ without (BCM = 0) or with 0.5 \times the MIC of BCM were determined (Extended Data Fig. 8). Histograms show the ratios ($\Delta rapA/wt$). Error bars denote the s.e.m. ($n = 3$ measurements). The statistical significance of differences between samples was determined using an unpaired, two-tailed t -test. **a**, Ratios of doubling times at matching conditions ($\Delta rapA/wt$). Data are presented as the best-fit values \pm s.e.m. (calculated from 95% confidence limits of best fit). **b**, Ratios of $t_{1/2}$ at matching conditions ($\Delta rapA/wt$). Data are presented as the best-fit values \pm s.e.m. (calculated from 95% confidence limits of best fit). **c**, The $\Delta rapA$ mutant cannot grow on LB plates + 1 M NaCl (top right) but overexpression of RNase HI enables growth (top left).

of the RNAs (Fig. 3d), confirming extensive production of R-loops. The RNase HI treatment reduced the peak of the RNA size distributions by about 4.8 ± 0.1 kb, corresponding to the size of the circular DNA template (Fig. 1a). This result supports the hypothesis that the core RNAPs transcribed all the way around the plasmid, generating an RNA–DNA hybrid the length of the DNA template. Further transcription would displace the RNA downstream of the RNAP from the DNA template, allowing the production of RNA transcripts longer than the DNA template but always leaving an RNA–DNA hybrid the length of the DNA template.

RapA contributes to the control of cytotoxic R-loops in vivo

Excessive PTCs on the DNA can lead to nonspecific transcription initiation and generate extensive R-loops (Fig. 3d). Excessive R-loop formation in vivo is a threat to genomic stability and can be lethal^{26,46–48}. We hypothesize that RapA may contribute to the control of R-loops

in vivo by removing PTCs, a potential source of R-loops. We first tested this hypothesis by comparing the growth of an *E. coli* *rapA*-null mutant ($\Delta rapA$) to the wild-type parent strain (wt) under conditions of R-loop stress (Extended Data Fig. 8), induced by growing the cells in the presence of bicyclomycin (BCM), a selective inhibitor of the Rho termination factor⁴⁹. Rho has an essential role in *E. coli* by suppressing R-loop formation^{47,50}. The cells carried pBAD18*rnhA* (a plasmid expressing *rnhA*, encoding *E. coli* RNase HI, under control of the arabinose-inducible P_{BAD} promoter)⁵¹ or the empty pBAD18 plasmid as a negative control. We reasoned that a growth defect of the $\Delta rapA$ strain under R-loop stress would be compensated for by overexpression of RNase HI through the induction of pBAD18*rnhA*, directly confirming the role of R-loops. We analyzed cell growth (monitored by the optical density at 600 nm (OD_{600})) using two parameters: the doubling time during log-phase growth and $t_{1/2}$, the time for the cells to reach half their OD_{600} plateau (Extended Data Fig. 8a–c).

In the absence of BCM, the $\Delta rapA$ strain had a small but reproducible growth defect (less than 1.2-fold) compared to wt under all conditions tested (Extended Data Fig. 8d,e). The growth rate defect of $\Delta rapA$ (relative to wt) increased significantly (doubling time, 1.3-fold; $t_{1/2}$, 1.7-fold) when the cells were grown in the presence of BCM at 0.5 \times the minimum inhibitory concentration (MIC) (Fig. 4a,b and Extended Data Fig. 8f,g). The increased growth defect of $\Delta rapA$ in the presence of BCM was corrected by the expression of RNase HI (Fig. 4a,b and Extended Data Fig. 8f,g).

To test the hypothesis that RapA contributes to the control of R-loops in vivo in distinct growth conditions and without the use of BCM, we took advantage of a previous finding that the deletion of *rapA* renders *E. coli* unable to grow on Luria–Bertani (LB) plates with 1 M NaCl (Fig. 4c)¹². The apparent lethality of 1 M NaCl to $\Delta rapA$ was rescued by expression of RNase HI (Fig. 4c). This points to a role for R-loop toxicity in the inability of $\Delta rapA$ to grow on 1 M NaCl.

E. coli responds to osmotic stress (such as 1 M NaCl in the surrounding medium) by accumulating high concentrations of osmolytes in the cytoplasm; major osmolytes include K^+ ions, glutamate and trehalose^{52,53}. These high concentrations of osmolytes can have notable effects on protein–DNA interactions⁵⁴. We suggest that the altered cytoplasmic conditions under osmotic stress may stabilize PTCs but that PTC accumulation is prevented by RapA activity in wt *E. coli*. In the absence of RapA, PTCs accumulate, leading to increased levels of PTC-mediated initiation and production of R-loops to a lethal level.

Discussion

Mechanisms underlying pervasive transcription initiation are of growing interest as genome-wide sequencing techniques have allowed deeper coverage of in vivo transcription to be achieved⁵⁵. The role of PTCs in the production of this promoter-independent transcription has been difficult to structurally probe because of challenging biochemical reconstitution constraints. PTCs exhibit one-dimensional diffusion on the DNA^{4–6} (meaning they could slide off the ends of a linear DNA fragment) and core RNAP binds tightly to the ends of linear DNA fragments²⁸. These features preclude the use of linear DNA fragments typically used in cryo-EM analyses of protein–DNA complexes. By reconstituting PTCs on a negatively supercoiled circular duplex DNA substrate, our results provide insight into the structural nature of PTCs and promoter-independent transcription initiation more broadly and the role of RapA in preventing the excessive buildup of PTCs, leading to a revised model for the bacterial transcription cycle (Fig. 5)⁴.

The σ -dependent transcription begins with base flipping and capture of conserved nt-strand bases (normally at positions –11 and –7 with respect to the transcription start site at +1)⁵⁶ within the –10 core promoter element, triggering transcription bubble nucleation and bubble propagation downstream to the transcription start site^{57,58}. Our rPTC structures show that core RNAP can bind and bend the DNA to nucleate a transcription bubble on negatively supercoiled DNA independent of

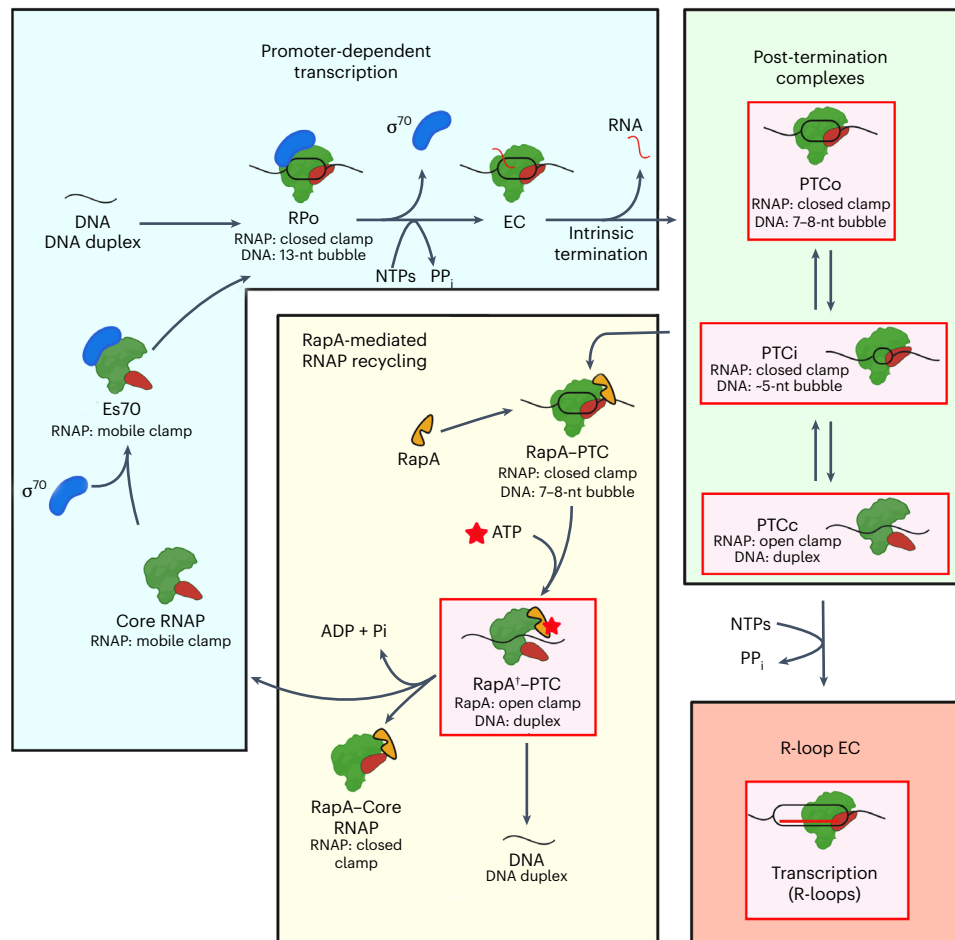


Fig. 5 | Model for the role of RapA in the bacterial transcription cycle.

Results from this work (highlighted in red-shaded boxes) yield a model for the role of RapA in the bacterial transcription cycle: (i) in promoter-dependent transcription (light-blue background), free core RNAP (green but with dark-red clamp) combines with σ^{70} (blue) to form Es 70 , which locates promoter DNA sequences and initiates promoter-specific transcription; (ii) following intrinsic termination, core RNAP can remain on the DNA in a PTC, equilibrating among PTC_o \rightleftharpoons PTC_i \rightleftharpoons PTC_c (light-green background); (iii) PTC_o can initiate

transcription independent of σ but is prone to cytotoxic R-loop formation (promoter-independent transcription, light-orange background); (iv) the toxic formation of R-loops is suppressed by RapA (orange), which specifically binds PTCs and pulls open the RNAP clamp in an ATP-dependent manner. This allows the transcription bubble to reanneal and remove the core RNAP from DNA, facilitating RNAP recycling and averting the harmful buildup of R-loops (RapA-mediated RNAP recycling, light-yellow background). Created with [BioRender.com](https://www.biorender.com).

the σ factor or conserved promoter elements (Fig. 1c–f). Core RNAP appears to nucleate its transcription bubble from within the RNAP active-site cleft and to propagate in the upstream direction while engaging SW2, FL2 and the β' rudder in the reverse order from σ -dependent transcription initiation (Extended Data Fig. 3).

Evolved strategies to suppress promoter-independent transcription appear manifold. Termination factor Rho targets ECs producing aberrant transcripts⁵⁹. Additional mechanisms for preventing nonspecific association of RNAP with DNA outside of promoter sequences include autoinhibitory σ^{70}_{11} (ref. 60), DNA packaging proteins (such as H-NS)⁶¹ and RapA⁷. Our approach for generating rPTCs suitable for cryo-EM analysis allowed us to visualize RapA engaged with its true target substrate (Fig. 2a). Our RapA[†]-PTC structure, along with comparisons to previously determined apo RapA–RNAP and apo RapA–EC structures, illustrate how nucleotide binding drives a complex allosteric conformational rearrangement of RapA that pulls open the RNAP clamp, allowing melted regions of the DNA to rewind and promoting dissociation of the DNA. Further work will be required to determine the role of ATP hydrolysis (as distinct from nucleotide binding) in the RapA functional cycle.

Dey et al.⁶² found that a population of *E. coli* RNAP ECs paused at the U-rich pause site following the HK022 putL element released their RNA transcript but remained associated with the DNA template (essentially

acting as PTCs). The RNAP conformation in these PTCs (PDB 8AC2 (ref. 62)) closely matches the rPTC_c RNAP conformation and both of these are very similar to the PTC portion of our RapA[†]-PTC structure (Supplementary Table 2). Thus, RapA uses ATP binding energy to stabilize a pre-existing PTC state. Dey et al.⁶² did not observe closed-clamp or open-bubble structures corresponding to rPTC_i or rPTC_o, presumably because their complexes were formed on linear DNA fragments that lacked supercoiling.

Our in vitro and in vivo results point to the formation of cytotoxic R-loops through σ^{70} -independent transcription mediated by PTCs (Figs. 3d and 4). Our in vivo experiments show that the overexpression of RNase HI rescues growth defects of a *rapA*-null strain ($\Delta rapA$) at two distinct growth conditions: R-loop stress induced by sub-MIC BCM (Fig. 4a,b and Extended Data Fig. 8) and osmotic stress induced by 1 M NaCl (Fig. 4c). As observed previously¹², the $\Delta rapA$ strain appeared to be completely unable to grow on LB agar + 1 M NaCl (Fig. 4c), suggesting that *rapA* may be essential under this condition (conditional essentiality). Strikingly, overexpressing RNase HI allowed growth at this otherwise lethal condition for the $\Delta rapA$ strain. This result strongly suggests that, under osmotic stress, the loss of RapA function leads to a lethal accumulation of R-loops, presumably generated by uncontrolled PTC-mediated initiation.

Our observation that σ^{70} -independent transcription initiation is prone to R-loop formation points to a crucial role for σ^{70} in initiating proper RNA transcript strand separation from the RNA–DNA hybrid during initial transcription at promoters. The σ^{70} family of σ factors¹ contain a conserved structural element, the σ -finger (also called the $\sigma^{70}_{3,2}$ -loop)^{63,64}, that loops into the RNAP cleft and helps preorganize the t-strand DNA near the active site but also blocks the path of the elongating nascent RNA^{63,64}. As the RNA chain extends during initiation, a steric clash with the σ -finger promotes abortive initiation or displaces the σ -finger, facilitating promoter escape^{63–66}. We hypothesize that the absence of the σ^{70} -finger in the RNAP cleft results in unsuccessful strand separation of the RNA–DNA hybrid during PTC transcription initiation. We stress, however, that the detailed molecular mechanism for R-loop generation by PTC-mediated nonspecific transcription initiation is immaterial to our main conclusions that (1) PTCs can initiate promoter-independent transcription and are prone to R-loop formation and (2) PTC-mediated promoter-independent initiation and R-loop formation are both suppressed by disruption of PTCs by RapA.

Microorganisms are ubiquitous across a vast assortment of environments and have consequently developed survival strategies for frequent osmotic shock⁵². *E. coli* has effectively solved the biophysical challenge of surviving in aqueous environments ranging from highly dilute solutions to those containing molar concentrations of salts⁵³. Here, our results highlight the lethal threat posed by cytotoxic R-loops and how the activity of RapA in evicting PTCs permits cell survival at the high osmotic strength of 1 M NaCl (Fig. 4c).

Altogether, our findings implicate transcription initiation by PTCs, either before or after the association of σ , in promoter-independent transcription and the generation of cytotoxic R-loops in bacteria. Additionally, our structure of RapA⁺-rPTC delineates the mechanisms underlying the suppression of promoter-independent transcription by RapA. We reveal a previously unappreciated role for RapA in vivo, contributing to the suppression of deleterious R-loops. RapA is spread widely among bacterial lineages but not universally so. We hypothesize that bacterial lineages that lack RapA may harbor analogous ATPases that fulfill similar roles to *E. coli* RapA^{67–70}. The behavior of bacterial RNAPs other than *E. coli* RNAP after intrinsic termination is unknown; further studies will be required to understand how the potential for promoter-independent transcription and R-loop accumulation is suppressed in bacteria that lack RapA.

Online content

Any methods, additional references, Nature Portfolio reporting summaries, source data, extended data, supplementary information, acknowledgements, peer review information; details of author contributions and competing interests; and statements of data and code availability are available at <https://doi.org/10.1038/s41594-024-01447-8>.

References

- Feklistov, A., Sharon, B. D., Darst, S. A. & Gross, C. A. Bacterial sigma factors: a historical, structural, and genomic perspective. *Annu. Rev. Microbiol.* **68**, 357–376 (2014).
- Mooney, R. A., Darst, S. A. & Landick, R. Sigma and RNA polymerase: an on-again, off-again relationship? *Mol. Cell* **20**, 335–345 (2005).
- Ray-Soni, A., Bellecourt, M. J. & Landick, R. Mechanisms of bacterial transcription termination: all good things must end. *Annu. Rev. Biochem.* **85**, 319–347 (2016).
- Harden, T. T. et al. Alternative transcription cycle for bacterial RNA polymerase. *Nat. Commun.* **11**, 448 (2020).
- Kang, W. et al. Transcription reinitiation by recycling RNA polymerase that diffuses on DNA after releasing terminated RNA. *Nat. Commun.* **11**, 450 (2020).
- Kang, W., Hwang, S., Kang, J. Y., Kang, C. & Hohng, S. Hopping and flipping of RNA polymerase on DNA during recycling for reinitiation after intrinsic termination in bacterial transcription. *Int. J. Mol. Sci.* **22**, 2398 (2021).
- Inlow, K., Tenenbaum, D., Friedman, L. J., Kondev, J. & Gelles, J. Recycling of bacterial RNA polymerase by the Swi2/Snf2 ATPase RapA. *Proc. Natl Acad. Sci. USA* **120**, e2303849120 (2023).
- Tenenbaum, D. et al. RNA polymerase sliding on DNA can couple the transcription of nearby bacterial operons. *Proc. Natl Acad. Sci. USA* **120**, e2301402120 (2023).
- Sukhodolets, M. V. & Jin, D. J. Interaction between RNA polymerase and RapA, a bacterial homolog of the SWI/SNF protein family. *J. Biol. Chem.* **275**, 22090–22097 (2000).
- Sukhodolets, M. V. & Jin, D. J. RapA, a novel RNA polymerase-associated protein, is a bacterial homolog of SWI2/SNF2. *J. Biol. Chem.* **273**, 7018–7023 (1998).
- Muzzin, O. et al. Disruption of *Escherichia coli* hepA, an RNA polymerase-associated protein, causes UV sensitivity. *J. Biol. Chem.* **273**, 15157–15161 (1998).
- Sukhodolets, M. V., Cabrera, J. E., Zhi, H. & Jin, D. J. RapA, a bacterial homolog of SWI2/SNF2, stimulates RNA polymerase recycling in transcription. *Gene Dev.* **15**, 3330–3341 (2001).
- Fleurier, S., Dapa, T., Tenaillon, O., Condon, C. & Matic, I. rRNA operon multiplicity as a bacterial genome stability insurance policy. *Nucleic Acids Res.* **50**, 12601–12620 (2022).
- Lynch, S. V. et al. Role of the *rapA* gene in controlling antibiotic resistance of *Escherichia coli* biofilms. *Antimicrob. Agents Chemother.* **51**, 3650–3658 (2007).
- Merrell, D. S., Hava, D. L. & Camilli, A. Identification of novel factors involved in colonization and acid tolerance of *Vibrio cholerae*. *Mol. Microbiol.* **43**, 1471–1491 (2002).
- Yawn, B., Zhang, L., Mura, C. & Sukhodolets, M. V. RapA, the SWI/SNF subunit of *Escherichia coli* RNA polymerase, promotes the release of nascent RNA from transcription complexes. *Biochemistry* **48**, 7794–7806 (2009).
- Stec-Dziedzic, E., Łyżeń, R., Skärffstad, E., Shingler, V. & Szalewska-Pałasz, A. Characterization of the transcriptional stimulatory properties of the *Pseudomonas putida* RapA protein. *Biochim. Biophys. Acta* **1829**, 219–230 (2013).
- Qayyum, M. Z., Molodtsov, V., Renda, A. & Murakami, K. S. Structural basis of RNA polymerase recycling by the SWI2/SNF2 family of ATPase RapA in *Escherichia coli*. *J. Biol. Chem.* **297**, 101404 (2021).
- Portman, J. R., Qayyum, M. Z., Murakami, K. S. & Strick, T. R. On the stability of stalled RNA polymerase and its removal by RapA. *Nucleic Acids Res.* **50**, 7396–7405 (2022).
- Liu, B., Zuo, Y. & Steitz, T. A. Structural basis for transcription reactivation by RapA. *Proc. Natl Acad. Sci. USA* **112**, 2006–2010 (2015).
- Shi, W. et al. Structural basis for activation of SWI2/SNF2 ATPase RapA by RNA polymerase. *Nucleic Acids Res.* **49**, 10707–10716 (2021).
- Shaw, G. et al. Structure of RapA, a SWI2/SNF2 protein that recycles RNA polymerase during transcription. *Structure* **16**, 1417–1427 (2008).
- Jin, D. J., Zhou, Y. N., Shaw, G. & Ji, X. Structure and function of RapA: a bacterial SWI2/SNF2 protein required for RNA polymerase recycling in transcription. *Biochim. Biophys. Acta* **1809**, 470–475 (2011).
- Nechaev, S. & Severinov, K. RapA: completing the transcription cycle? *Structure* **16**, 1294–1295 (2008).
- Wittinghofer, A. Signaling mechanistics: aluminum fluoride for molecule of the year. *Curr. Biol.* **7**, R682–R685 (1997).

26. Belotserkovskii, B. P., Tornaletti, S., D'Souza, A. D. & Hanawalt, P. C. R-loop generation during transcription: formation, processing and cellular outcomes. *DNA Repair* **71**, 69–81 (2018).
27. Wade, J. T. & Grainger, D. C. Pervasive transcription: illuminating the dark matter of bacterial transcriptomes. *Nat. Rev. Microbiol.* **12**, 647–653 (2014).
28. Melancon, P., Burgess, R. R. & Record, M. T. Direct evidence for the preferential binding of *Escherichia coli* RNA polymerase holoenzyme to the ends of deoxyribonucleic acid restriction fragments. *Biochemistry* **22**, 5169–5176 (1983).
29. Scheres, S. H. W. RELION: implementation of a Bayesian approach to cryo-EM structure determination. *J. Struct. Biol.* **180**, 519–530 (2012).
30. Kang, J. Y. et al. An ensemble of interconverting conformations of the elemental paused transcription complex creates regulatory options. *Proc. Natl Acad. Sci. USA* **120**, e2215945120 (2023).
31. Chakraborty, A. et al. Opening and closing of the bacterial RNA polymerase clamp. *Science* **337**, 591–595 (2012).
32. Lane, W. J. & Darst, S. A. Molecular evolution of multisubunit RNA polymerases: structural analysis. *J. Mol. Biol.* **395**, 686–704 (2010).
33. Naji, S., Bertero, M. G., Spitalny, P., Cramer, P. & Thomm, M. Structure–function analysis of the RNA polymerase cleft loops elucidates initial transcription, DNA unwinding and RNA displacement. *Nucleic Acids Res.* **36**, 676–687 (2007).
34. Pupov, D. et al. Multiple roles of the RNA polymerase β' SW2 region in transcription initiation, promoter escape, and RNA elongation. *Nucleic Acids Res.* **38**, 5784–5796 (2010).
35. Kuznedelov, K., Korzheva, N., Mustaev, A. & Severinov, K. Structure-based analysis of RNA polymerase function: the largest subunit's rudder contributes critically to elongation complex stability and is not involved in the maintenance of RNA–DNA hybrid length. *EMBO J.* **21**, 1369–1378 (2002).
36. Kang, J. Y. et al. RNA polymerase accommodates a pause RNA hairpin by global conformational rearrangements that prolong pausing. *Mol. Cell* **69**, 802–815 (2018).
37. Guo, X. et al. Structural basis for NusA stabilized transcriptional pausing. *Mol. Cell* **69**, 816–827 (2018).
38. Zhu, C. et al. Transcription factors modulate RNA polymerase conformational equilibrium. *Nat. Commun.* **13**, 1546 (2022).
39. Hauk, G., McKnight, J. N., Nodelman, I. M. & Bowman, G. D. The chromodomains of the Chd1 chromatin remodeler regulate DNA access to the ATPase motor. *Mol. Cell* **39**, 711–723 (2010).
40. Ye, J., Osborne, A. R., Groll, M. & Rapoport, T. A. RecA-like motor ATPases—lessons from structures. *Biochim. Biophys. Acta* **1659**, 1–18 (2004).
41. Krissinel, E. & Henrick, K. Inference of macromolecular assemblies from crystalline state. *J. Mol. Biol.* **372**, 774–797 (2007).
42. Buckstein, M. H., He, J. & Rubin, H. Characterization of nucleotide pools as a function of physiological state in *Escherichia coli*. *J. Bacteriol.* **190**, 718–726 (2008).
43. Grigорова, I. L., Phleger, N. J., Mutalik, V. K. & Gross, C. A. Insights into transcriptional regulation and σ competition from an equilibrium model of RNA polymerase binding to DNA. *Proc. Natl Acad. Sci. USA* **103**, 5332–5337 (2006).
44. Mishra, R. K., Gopal, V. & Chatterji, D. Correlation between the DNA supercoiling and the initiation of transcription by *Escherichia coli* RNA polymerase in vitro: role of the sequences upstream of the promoter region. *FEBS Lett.* **260**, 273–276 (1990).
45. Daubendiek, S. L. & Kool, E. T. Generation of catalytic RNAs by rolling transcription of synthetic DNA nanocircles. *Nat. Biotechnol.* **15**, 273–277 (1997).
46. Kogoma, T. Stable DNA replication: interplay between DNA replication, homologous recombination, and transcription. *Microbiol. Mol. Biol. Rev.* **61**, 212–238 (1997).
47. Gowrishankar, J., Leela, J. K. & Anupama, K. R-loops in bacterial transcription. *Biochem. Soc. Symp.* **4**, 153–157 (2013).
48. Wimberly, H. et al. R-loops and nicks initiate DNA breakage and genome instability in non-growing *Escherichia coli*. *Nat. Commun.* **4**, 2115 (2013).
49. Zwiefka, A., Kohn, H. & Widger, W. R. Transcription termination factor rho: the site of bicyclomycin inhibition in *Escherichia coli*. *Biochemistry* **32**, 3564–3570 (1993).
50. Leela, J. K., Syeda, A. H., Anupama, K. & Gowrishankar, J. Rho-dependent transcription termination is essential to prevent excessive genome-wide R-loops in *Escherichia coli*. *Proc. Natl Acad. Sci. USA* **110**, 258–263 (2012).
51. Usongo, V. et al. Depletion of RNase HI activity in *Escherichia coli* lacking DNA topoisomerase I leads to defects in DNA supercoiling and segregation. *Mol. Microbiol.* **69**, 968–981 (2008).
52. Wood, J. M. Bacterial responses to osmotic challenges. *J. Gen. Physiol.* **145**, 381–388 (2015).
53. Record, M. T. Jr, Courtenay, E. S., Cayley, D. S. & Guttman, H. J. Responses of *E. coli* to osmotic stress: large changes in amounts of cytoplasmic solutes and water. *Trends Biochem. Sci.* **23**, 143–148 (1998).
54. Record, M. T. Jr, Zhang, W. & Anderson, C. F. Analysis of effects of salts and uncharged solutes on protein and nucleic acid equilibria and processes: a practical guide to recognizing and interpreting polyelectrolyte effects, Hofmeister Effects, and osmotic effects of salts. *Adv. Protein Chem.* **51**, 281–353 (1998).
55. Haas, B. J., Chin, M., Nusbaum, C., Birren, B. W. & Livny, J. How deep is deep enough for RNA-Seq profiling of bacterial transcriptomes? *BMC Genomics* **13**, 734 (2012).
56. Shultzaberger, R. K., Chen, Z., Lewis, K. A. & Schneider, T. D. Anatomy of *Escherichia coli* σ^{70} promoters. *Nucleic Acids Res.* **35**, 771–788 (2007).
57. Chen, J. et al. Stepwise promoter melting by bacterial RNA polymerase. *Mol. Cell* **78**, 275–288 (2020).
58. Feklistov, A. & Darst, S. A. Structural basis for promoter –10 element recognition by the bacterial RNA polymerase σ subunit. *Cell* **147**, 1257–1269 (2011).
59. Peters, J. M. et al. Rho and NusG suppress pervasive antisense transcription in *Escherichia coli*. *Gene Dev.* **26**, 2621–2633 (2012).
60. Bae, B. et al. Phage T7 Gp2 inhibition of *Escherichia coli* RNA polymerase involves misappropriation of σ^{70} domain 1.1. *Proc. Natl Acad. Sci. USA* **110**, 19772–19777 (2013).
61. Grainger, D. C. Structure and function of bacterial H-NS protein. *Biochem. Soc. Trans.* **44**, 1561–1569 (2016).
62. Dey, S. et al. Structural insights into RNA-mediated transcription regulation in bacteria. *Mol. Cell* **82**, 3885–3900 (2022).
63. Zhang, Y. et al. Structural basis of transcription initiation. *Science* **338**, 1076–80 (2012).
64. Murakami, K. S., Masuda, S. & Darst, S. A. Structural basis of transcription initiation: RNA polymerase holoenzyme at 4 Å resolution. *Science* **296**, 1280–1284 (2002).
65. Kulbachinskiy, A. & Mustaev, A. Region 3.2 of the subunit contributes to the binding of the 3'-initiating nucleotide in the RNA polymerase active center and facilitates promoter clearance during initiation. *J. Biol. Chem.* **281**, 18273–18276 (2006).
66. Li, L., Molodtsov, V., Lin, W., Ebricht, R. H. & Zhang, Y. RNA extension drives a stepwise displacement of an initiation-factor structural module in initial transcription. *Proc. Natl Acad. Sci. USA* **117**, 5801–5809 (2020).
67. Pei, H.-H. et al. The δ subunit and NTPase HelD institute a two-pronged mechanism for RNA polymerase recycling. *Nat. Commun.* **11**, 6418 (2020).
68. Newing, T. P. et al. Molecular basis for RNA polymerase-dependent transcription complex recycling by the helicase-like motor protein HelD. *Nat. Commun.* **11**, 6420 (2020).

69. Hurst-Hess, K. R., Saxena, A., Rudra, P., Yang, Y. & Ghosh, P. *Mycobacterium abscessus* HelR interacts with RNA polymerase to confer intrinsic rifamycin resistance. *Mol. Cell* **82**, 3166–3177 (2022).
70. Surette, M. D., Waglechner, N., Koteva, K. & Wright, G. D. HelR is a helicase-like protein that protects RNA polymerase from rifamycin antibiotics. *Mol. Cell* **82**, 3151–3165 (2022).
71. Kang, J. Y. et al. Structural basis of transcription arrest by coliphage HK022 nun in an *Escherichia coli* RNA polymerase elongation complex. *eLife* **6**, e25478 (2017).
72. Cardone, G., Heymann, J. B. & Steven, A. C. One number does not fit all: mapping local variations in resolution in cryo-EM reconstructions. *J. Struct. Biol.* **184**, 226–236 (2013).
73. Briat, J. F. & Chamberlin, M. J. Identification and characterization of a new transcriptional termination factor from *Escherichia coli*. *Proc. Natl Acad. Sci. USA* **81**, 7373–7377 (1984).
74. Guzman, L. M., Belin, D., Carson, M. J. & Beckwith, J. Tight regulation, modulation, and high-level expression by vectors containing the arabinose P_{BAD} promoter. *J. Bacteriol.* **177**, 4121–4130 (1995).

Publisher's note Springer Nature remains neutral with regard to jurisdictional claims in published maps and institutional affiliations.

Springer Nature or its licensor (e.g. a society or other partner) holds exclusive rights to this article under a publishing agreement with the author(s) or other rightsholder(s); author self-archiving of the accepted manuscript version of this article is solely governed by the terms of such publishing agreement and applicable law.

© The Author(s), under exclusive licence to Springer Nature America, Inc. 2025

Methods

Structural biology software was accessed through the SBGrid consortium⁷⁵. No statistical methods were used to predetermine sample size. The experiments were not randomized. The investigators were not blinded to allocation during experiments and outcome assessment.

Protein expression, purification, reconstitution and labeling

E. coli core RNAP and σ^{70} were separately overexpressed and purified as previously described⁵⁷. Briefly, a pET-based plasmid overexpressing each subunit of *E. coli* RNAP (full-length α , β and ω) and β' -PPX-His10 (PPX; PreScission protease site, LEVLFGQP, Cytiva) was cotransformed with a pACYCDuet-1 plasmid containing *E. coli* *rpoZ* (encoding ω) into *E. coli* BL21(DE3) (Novagen). Protein expression was induced with 1 mM IPTG for 4 h at 30 °C. Cells were harvested and lysed with a French Press (Avestin) at 4 °C. Lysate was precipitated using polyethyleneimine (PEI; 10% (w/v), pH 8.0; Acros Organics). Pellets were washed and RNAP was eluted. The PEI elutions were precipitated with ammonium sulfate. Pellets were harvested, resuspended and loaded on to HiTrap IMAC HP columns (Cytiva) for purification by nickel affinity chromatography. Bound RNAP was washed on column, eluted and dialyzed. Dialyzed RNAP was loaded onto a Biorex-70 column (Bio-Rad) for purification by ion-exchange chromatography. Eluted RNAP was concentrated by centrifugal filtration and then loaded onto a HiLoad 26/600 Superdex 200 column (Cytiva) for purification by size-exclusion chromatography. Purified RNAP was supplemented with glycerol to 20% (v/v), flash-frozen in liquid N₂ and stored at -80 °C.

A plasmid encoding *E. coli* His₁₀-SUMO- σ^{70} was transformed into *E. coli* BL21(DE3) (Novagen). Protein expression was induced with 1 mM IPTG for 1 h at 30 °C. Cells were harvested and lysed with a French Press (Avestin) at 4 °C. Lysate was loaded onto a HiTrap IMAC HP column (Cytiva) for purification by nickel affinity chromatography. Eluted σ^{70} was cleaved with ULPI SUMO protease (Thermo Fisher Scientific) to remove the His₁₀-SUMO-tag from σ^{70} , followed by dialysis. The cleaved sample was further purified on a HiTrap IMAC HP column (Cytiva). Tagless σ^{70} was collected in the flowthrough and concentrated by centrifugal filtration. The sample was then loaded onto a HiLoad 16/60 Superdex 200 for purification by size-exclusion chromatography. Purified σ^{70} was supplemented with glycerol to a final concentration of 20% (v/v), flash-frozen in liquid N₂ and stored at -80 °C.

E. coli core RNAP containing a SNAP tag on the C terminus of β' (ref. 76) was fluorescently labeled with SNAP-Surface DY-549 dye (New England Biolabs), yielding wt RNAP⁵⁴⁹ as described previously⁴. Briefly, RNAP-SNAP was dialyzed into labeling buffer (10 mM Tris-HCl pH 8.0, 40 mM KCl, 5 mM MgCl₂, 20 μ M ZnCl₂ and 1 mM DTT) at 4 °C for 4 h. The resulting product was then mixed with equimolar SNAP-Surface DY-549 (1 mM in DMSO) at room temperature for 30 min. The product was mixed with an equal volume of labeling buffer supplemented with 60% glycerol (v/v) to yield RNAP⁵⁴⁹ in reconstitution buffer (10 mM Tris-HCl pH 8.0, 30% glycerol (v/v), 0.1 mM EDTA, 100 mM NaCl, 20 mM KCl, 20 μ M ZnCl₂, 3 mM MgCl₂ and 0.6 mM DTT), then flash-frozen and stored at -80 °C. A SNAP-tagged β' ZBD deletion mutant (Δ ZBD RNAP⁵⁴⁹; β' residues 64–94 replaced with a GS linker) was similarly purified and labeled. Native mass spectrometry (nMS) analysis of unlabeled SNAP-RNAP-SNAP samples showed that the wt RNAP-SNAP was mostly assembled core (80%); by contrast, only 9% of Δ ZBD RNAP-SNAP was fully assembled with 85% of the mutant core RNAP lacking the ω subunit. To avoid potential issues because of the low abundance of ω in Δ ZBD RNAP-SNAP, wt RNAP-SNAP and Δ ZBD RNAP-SNAP were labeled with DY-549 dye as above and then incubated with threefold and fourfold excess ω subunit, respectively. For wt RNAP⁵⁴⁹, 12 μ M wt RNAP⁵⁴⁹ was mixed with 36 μ M ω subunit and incubated on ice for 30 min. For Δ ZBD RNAP⁵⁴⁹, 1.83 μ M Δ ZBD RNAP⁵⁴⁹ was mixed with 7.68 μ M ω subunit and incubated on ice for 30 min. The samples were then buffer-exchanged into 10 mM Tris-HCl pH 8, 100 mM NaCl, 2.5 mM MgCl₂, 1 mM DTT and 25% glycerol (v/v) using Centri-Spin10 5-kDa spin columns (Princeton

Separations) and stored at -80 °C. Subsequent nMS analysis revealed that both wt RNAP⁵⁴⁹ and Δ ZBD RNAP⁵⁴⁹ core complexes were fully assembled and completely labeled with DY-549.

E. coli RapA was overexpressed and purified as previously described⁷. Briefly, *E. coli* RapA protein was overexpressed in *E. coli* BL21(DE3) cells transformed with pQE80L (Qiagen) expression vector (encoding N-terminally His₆-tagged full-length RapA)²² and grown in LB medium with ampicillin (100 μ g ml⁻¹) at 37 °C. Expression of RapA was induced with 1 mM IPTG; the cells were shaken at 37 °C and harvested after 3 h. RapA protein was purified by affinity and size-exclusion chromatography using prepacked 5-ml Ni-affinity (HisTrap HP), 5-ml heparin (HiTrap Heparin) and Superdex 200 columns (Cytiva) and stored in storage buffer (10 mM HEPES pH 7.5, 50 mM NaCl, 0.1 mM EDTA pH 8.0 and 5 mM DTT) at -80 °C. The fluorescently labeled SNAP-RapA construct, RapA⁶⁵⁰, was prepared as previously described⁷. Plasmid pK11 (Addgene, 199118) encoding His₆-SNAP-RapA was transformed into NEBExpressIQ cells (New England Biolabs) and the His₆-SNAP-RapA protein was expressed and purified as above. To make RapA⁶⁵⁰, His₆-SNAP-RapA and JFX-650 fluorophore SNAP substrate (kind gift from L. Lavis, Janelia Farm Research Campus) were mixed in a 1:2 molar ratio with 1 mM DTT in SNAP reaction buffer (50 mM Tris-HCl pH 7.5, 100 mM NaCl and 0.05% Tween-20). Excess dye was removed using an Ultra 0.5-ml 30-kDa spin column (Amicon). Purified RapA⁶⁵⁰ was frozen in liquid N₂ and stored at -80 °C in 10 mM Tris-HCl pH 7.9, 50% glycerol (v/v), 0.1 mM EDTA, 0.1 M NaCl and 1 mM DTT. The functionality of RapA⁶⁵⁰ compared to His₆-RapA was verified through single-molecule washout experiments⁷.

nMS analysis

The RNAP samples were buffer-exchanged into nMS solution (500 mM ammonium acetate pH 7.5 and 0.01% Tween-20) using Zeba microspin desalting columns (Thermo Fisher Scientific) with a 40-kDa molecular weight cutoff (MWCO)⁷⁷. For nMS analysis, 2–3 μ l of the buffer-exchanged sample was loaded into a gold-coated quartz emitter that was prepared in-house and then electrosprayed into an Exactive Plus extended mass range (EMR) instrument (Thermo Fisher Scientific) with a static nanospray source⁷⁸. The nMS parameters used were as follows: spray voltage, 1.2 kV; capillary temperature, 125–150 °C; in-source dissociation, 10 V; S-lens radiofrequency level, 200; resolving power, 8,750 or 17,500 at $m/z = 200$; automatic gain control target, 1×10^6 ; maximum injection time, 200 ms; number of microscans, 5; injection flatapole, 8 V; interflatapole, 4 V; bent flatapole, 4 V; high-energy collision dissociation, 200 V; ultrahigh vacuum pressure, $5.5\text{--}6.5 \times 10^{-10}$ mbar; total number of scans, at least 100. Mass calibration in positive EMR mode was performed using cesium iodide. The acquired MS spectra were visualized using Thermo Xcalibur Qual Browser (version 4.2.47) and processed further using the deconvolution software UniDec (version 4.2.0)^{79,80} to obtain the deconvolved masses. The resulting measured masses for the unlabeled SNAP-RNAP assemblies observed included the wt core at 412,045 Da, wt core- ω at 402,035 Da, $\alpha_2\beta$ at 223,691 Da, β' Δ ZBD core at 408,544 Da and β' Δ ZBD core- ω at 398,427 Da. The measured masses for the DY-549-labeled SNAP-RNAP assemblies incubated with excess ω subunit included wt RNAP⁵⁴⁹ at 413,105 Da and β' Δ ZBD RNAP⁵⁴⁹ at 409,687 Da, which closely matched the mass of the corresponding RNAP core with one covalently attached DY-549 dye. The mass accuracies, calculated as the percentage mass deviation between the measured and predicted masses, ranged from 0.03% to 0.07%.

DNA templates

The initial discovery and characterization of PTCs by single-molecule analysis used linear DNA templates^{4,5} but subsequent experiments characterizing PTCs used promoterless circular DNA templates⁸, including a small 586-bp promoterless circular DNA template used in single-molecule studies of RapA function⁷. The single-molecule

studies herein (Fig. 2e) used this same 586-bp circular DNA template. Direct comparison of the results from all of the experiments described herein (single-molecule, cryo-EM and in vitro transcription) using the same DNA template would be ideal, but the 586-bp circular DNA template could not be generated in sufficient yield for the cryo-EM experiments and we sought to use an in vitro transcription DNA template containing the well-characterized T7A1 promoter and terminator to facilitate a comparison of $E\sigma^{70}$ and E transcription characteristics. The rationale for the various DNA templates and their construction is described below.

In vitro transcription reactions. We used the 4.8-kb plasmid pARI707 (ref. 73) containing the strong T7A1 promoter and terminator (Fig. 3a). This facilitated direct comparison of the in vitro transcription reactions using $E\sigma^{70}$ or E; in contrast to E, $E\sigma^{70}$ was expected to yield an easily identifiable 161-nt transcript (Fig. 3c).

To test that the presence of the strong T7A1 promoter (or other promoters) on pARI707 did not influence our analysis of rPTCs, we generated a derivative of pARI707 (pJB2) in which all of the annotated promoters⁷¹ (<https://www.ncbi.nlm.nih.gov/nuccore/J01749>) were removed, with the exception of the weak *pbla* promoter required for ampicillin resistance (Extended Data Fig. 7a,b).

Cryo-EM. We reasoned that preparing cryo-EM grids for single-particle data collection would be facilitated by a smaller circular DNA template. Because we could not generate the 586-bp circular DNA template (used in the single-molecule experiments) in sufficient yield for the cryo-EM experiments, we constructed pJB1 (1.9-kb plasmid instead of 4.9-kb pARI707; Fig. 1a) using Gibson assembly on amplicons generated from plasmids pARI707 and pUC57. The pARI707 insert amplicon contains a T7A1 promoter sequence and downstream 21-mer stall sequence derived from pARI707 (for use outside of the scope of this work). The pUC57 backbone amplicon included an ampicillin resistance gene and a high-copy-number origin of replication.

Preparation of *E. coli* rPTC complex for cryo-EM. *E. coli* core RNAP (0.5 ml of 5 mg ml⁻¹ protein) was injected into a 10/300 Superose 6 Increase column (Cytiva) equilibrated with 10 mM Tris-HCl pH 8.0, 100 mM KCl, 5 mM MgCl₂ and 2.5 mM DTT. The peak fractions of the eluted protein were concentrated by centrifugal filtration (EMD Millipore, 30-kDa MWCO) to 25 μM protein concentration.

Plasmid pJB1 was grown overnight in DH5α cells in standard Luria broth with 100 μg ml⁻¹ ampicillin and isolated using a plasmid DNA maxiprep kit (Qiagen). Plasmid DNA solution at 1,750 ng μl⁻¹ was added to core RNAP for a final concentration of 491 ng μl⁻¹ DNA (0.82 μM). The sample was incubated for 15 min at 37 °C; then, CHAPSO (Anatrace) was added to a final concentration of 8 mM (ref. 81) and the sample was kept at room temperature before grid preparation.

Preparation of RapA-rPTC complex for cryo-EM. The rPTC complexes were prepared as described above but with the plasmid final concentration of 0.42 μM. RapA (20 μM) was preincubated with AIF₃ and ADP (2.5 mM each) (Sigma-Aldrich). The ADP-AIF₃-RapA solution was added to the rPTC sample to achieve a final concentration of 8 μM RapA, 1 mM AIF₃ and 1 mM ADP. CHAPSO was then added (8 mM final concentration) and the sample was kept at room temperature before grid preparation.

Cryo-EM grid preparation

C-flat holey carbon grids (CF-1.2/1.3-4Au; Protochips) were glow-discharged for 20 s before the application of 3.5 μl of the sample (0.42 μM plasmid DNA, 8 μM core RNAP, 8 μM RapA, 1 mM ADP, 1 mM AIF₃ and 8 mM CHAPSO). After blotting for 3–4.5 s the grids were plunge-frozen in liquid ethane using an FEI Vitrobot Mark IV (FEI) with 100% chamber humidity at 37 °C.

Cryo-EM data acquisition and processing

***E. coli* rPTCs.** Grids were imaged using a 300-keV Titan Krios (FEI) equipped with a K3 Summit direct electron detector (Gatan). Images were recorded with Legikon⁸² in counting mode with a pixel size of 1.076 Å and a defocus range of –0.25 to –4.16 μm. Data were collected with a dose rate of 28 e⁻ per Å² per second. Images were recorded over a 2-s exposure with 0.05-s frames (40 total frames) to give a total dose of 55.9 e⁻ per Å². Dose-fractionated videos were gain-normalized, drift-corrected, summed and dose-weighted using MotionCor2 (ref. 83). The contrast transfer function (CTF) was estimated for each summed image using the Patch CTF module in cryoSPARC3 (CS3)⁸⁴. Particles were picked and extracted from the dose-weighted images with a box size of 256 pixels using CS3 blob picker and particle extraction. Coordinates pointing to contaminating ice particles were extracted as faux particles and used to generate an initial decoy 3D model in CS3 (ab initio reconstruction) to remove junk particles from initial particle stacks. Multiple rounds of CS3 hetero refinement of all blob-picked particles using 3D templates from this 3D decoy along with an *E. coli* core RNAP 3D template (PDB 6ALH with all nucleic acids removed, lowpass-filtered to 20-Å resolution) were used to identify a 3D consensus reconstruction containing subclasses for rPTCo and rPTCi. Multiple rounds of CS3 hetero refinement of all blob-picked particles using 3D templates of the 3D decoy along with *E. coli* core RNAP 3D template (PDB 6GH6 with all nucleic acids removed, lowpass-filtered to 20-Å resolution) were used to identify a 3D consensus reconstruction containing the subclass for rPTCc. Many classification schemes were tested that converged on the conclusion that three mid-to-high-resolution classes were present in the particle dataset. All three classes were subjected to two rounds of successive Bayesian polishing in RELION-3 (ref. 85). CS3 CTF refinement and nonuniform refinement were then performed for each resulting class, yielding three distinct structures: rPTCc (13,101 particles, 4.7-Å nominal resolution), rPTCi (49,701 particles, 3.8-Å nominal resolution) and rPTCo (86,865 particles, 3.6-Å nominal resolution) (Extended Data Figs. 1 and 2).

***E. coli* rPTC+RapA.** Grids were initially screened using a 200-keV Talos Arctica (FEI) equipped with a K2 Summit direct electron detector. Datasets were recorded with a pixel size of 1.5 Å over a defocus range of –1.0 to –3.5 μm. Videos were recorded in counting mode at 8 e⁻ per physical pixel per second in dose fractionation mode with subframes of 0.3 s over a 15-s exposure (50 frames) to give a total dose of 53.33 e⁻ per Å². Dose-fractionated videos were gain-normalized, drift-corrected, summed and dose-weighted using MotionCor2 (ref. 83). The CTF was estimated for each summed image using the Patch CTF module in CS3 (ref. 84). Particles were picked and extracted from the dose-weighted images with a box size of 256 pixels using CS3 blob picker and particle extraction. Particles were curated by CS3 2D classification and selection. CS3 ab initio reconstruction was used to produce a density map of rPTC + RapA. CS3 nonuniform refinement was used to further refine this initial map to 6.16 Å. Core RNAP subunits (no nucleic acids present) and all RapA domains, except for the spacer domain, were rigid-body refined to fit the density of the map. The resulting incomplete molecular model was used to produce a simulated 20-Å resolution density map for downstream templating.

For our full data collection, grids were imaged using a 300-keV Titan Krios (FEI) equipped with a K3 Summit direct electron detector (Gatan). Images were recorded with Legikon⁸² in counting mode with a pixel size of 1.076 Å and a defocus range of –0.8 to –2.5 μm. Data were collected with a dose rate of 26 e⁻ per Å² per second. Images were recorded over a 2-s exposure with 0.05-s frames (40 total frames) to give a total dose of 56 e⁻ per Å². Dose-fractionated videos were gain-normalized, drift-corrected, summed and dose-weighted using MotionCor2 (ref. 83). The CTF was estimated for each summed image using the Patch CTF module in CS4 (ref. 84). Particles were picked and extracted from the dose-weighted images with a box size of 256 pixels

using CS3 blob picker and particle extraction. An initial decoy 3D model was generated in CS4 (ab initio reconstruction) as described above. Multiple rounds of CS4 hetero refinement of all blob-picked particles using 3D templates of this 3D decoy along with the incomplete 20-Å ab initio map mentioned above (all nucleic acids and RapA spacer domain missing) were used to identify a 3D consensus reconstruction containing rPTC + RapA. This class was subjected to focused CS4 3D classification, masking around RapA to identify a clear class for RapA⁺-PTC. Then, two rounds of successive Bayesian polishing were performed in RELION-3 (ref. 85). Then, CS4 CTF refinement and nonuniform refinement were performed, yielding RapA⁺-PTC from 100,010 particles at 3.6-Å nominal resolution (Extended Data Fig. 5b,c).

The heat map distributions of particle orientations and half-map Fourier shell correlations (FSCs) were calculated using CS3. The 3D Fourier shell correlation calculations were performed using 3DFSC (ref. 86). Local resolution calculations were performed using blocres and maps were locally filtered using blocfilt (Bsoft package)⁷².

Model building and refinement

rPTCs. The initial model for the rPTCs was derived from PDB 8EG7 (ref. 30) with all of the nucleic acids removed. The model was manually fit into the cryo-EM density maps using ChimeraX⁸⁷ and rigid-body and real-space refined using PHENIX real_space_refine^{88,89}. For real-space refinement, rigid-body refinement was followed by all-atom and B-factor refinement with Ramachandran and secondary-structure restraints. Models were inspected and modified using Coot⁹⁰.

RapA⁺-PTC. The initial model for RapA⁺-PTC included the rPTC model (determined herein) combined with RapA from PDB 7M8E (ref. 21). Steps of model building and refinement followed the same steps for the rPTCs described above.

Single-molecule experiments

Construction of the 586-bp circular promoterless DNA template (npDNA^{Cy5}) used in single-molecule experiments was performed as described previously⁷. In brief, a PCR product (template for Golden Gate assembly, described below) was amplified from pDT4 (Addgene, 199120) using primers 5'-GAA GGT CTC CAG CCG TAC CAA CCA GCG GCT TAT C-3' and 5'-CCG GGT CTC ACC ATA CCC GCT GTC TGA GAT TAC G-3'. The npDNA^{Cy5} template was then made by BsaI Golden Gate assembly (New England Biolabs, Golden Gate assembly mix) in T4 DNA ligase buffer using equimolar PCR product and a synthetic duplex oligonucleotide containing internal biotin and Cy5 dye modifications made by annealing the complementary DNAs 5'-CGA TTA GGT CTC GGG CTA GTA CTG GTT TCT AGA G/iCy5/GT TCC AAG CC/iBio/ TCA CGG CGG CCG CCC ATC GAG ACC GGT TAA CC-3' and 5'-GGT TAA CCG GTC TCG ATG GGC GGC CGC CGT GAG GCT TGG AAC CTC TAG AAA CCA GTA CTA GCC CGA GAC CTA ATC G-3' (Integrated DNA Technologies). Reactions were incubated for alternating cycles of 5 min at 37 °C and 10 min at 16 °C, followed by 5 min at 55 °C and then 10 min at 65 °C to inactivate T4 DNA ligase. The product was digested with 10 U of T5 exonuclease (New England Biolabs) for 30 min at 37 °C, followed by inactivation with 15 mM EDTA, and further purified with the Qiaquick PCR purification kit (Qiagen).

Single-molecule fluorescence experiments were set up as described previously⁷. Briefly, we used a micromirror TIRF instrument with a ~65-µm-diameter circular field of view. We used excitation wavelengths 532 nm to monitor RNAP⁵⁴⁹ and 633 nm to locate DNA^{Cy5}. The temperature of the reaction chamber was maintained at 33.1 ± 0.5 °C using a custom temperature control system. Single-molecule observations were performed in glass flow chambers (volume ~20 µl) passivated with succinimidyl (NHS) polyethylene glycol (PEG) and NHS-PEG-biotin (Laysan Bio). Streptavidin (21125, Life Technologies) was introduced at 220 nM in wash buffer (50 mM Tris-acetate pH 8.0, 100 mM potassium acetate, 8 mM magnesium acetate, 27 mM ammonium acetate and 0.1 mg ml⁻¹

BSA (126615, EMB Chemicals)), incubated for 1 min and washed out (all washout steps used two flushes each of four chamber volumes of wash buffer). Streptavidin-coated fluorescent beads (T-10711, Molecular Probes), used as markers for stage drift correction, were loaded in the chamber at a dilution of ~1:400,000 and excess beads were washed out. The chamber was then incubated with 25 pM npDNA^{Cy5} in wash buffer for 5 min and excess npDNA^{Cy5} was flushed. Locations of surface-tethered npDNA^{Cy5} molecules were recorded by acquiring five 1-s exposure images with 633-nm excitation at a power of 400 µW (all laser powers measured incident to the objective lens). Next, we introduced either 1.5 nM RNAP⁵⁴⁹ or 4 nM ΔZBD RNAP⁵⁴⁹ into the chamber in transcription buffer (wash buffer supplemented with 3.5% w/v PEG8000 (81268, Sigma-Aldrich), 1 mg ml⁻¹ BSA and an O₂-scavenging system (4.5 mg ml⁻¹ glucose, 40 U per ml glucose oxidase, 1,500 U per ml catalase and 1 mM DTT)), incubated for 10 min to allow binding to npDNA^{Cy5} and rPTC formation, and washed out to remove excess unbound RNAP⁵⁴⁹. Then, solutions of wash buffer, 5 nM RapA⁶⁵⁰ or 5 nM RapA⁶⁵⁰ + 1 mM ATP were mixed in transcription buffer and loaded into the glass chamber. Image acquisition began within 10 s after loading the reagents (at *t* = 0), with excitation alternating between 532 and 633 nm (400 µW each) at one frame per second for 40 min. Lifetimes (*τ*) of RNAP⁵⁴⁹ and ΔZBD RNAP⁵⁴⁹ on npDNA^{Cy5} were determined by measuring the intervals where RNAP⁵⁴⁹ or ΔZBD RNAP⁵⁴⁹ was present on DNA⁷.

Transcription assays

Eσ⁷⁰ was reconstituted by incubating core RNAP (0.5 µM final) with σ⁷⁰ (2.5 µM final) at 37 °C for 15 min. Either core RNAP or Eσ⁷⁰ (as indicated) was incubated with ATP, cytidine triphosphate, guanosine triphosphate and uridine triphosphate (500 µM each; TriLink Biotechnologies) and pAR1707 (ref. 73) (35.8 nM final; Fig. 3a) or pJB2 (41.1 nM final; Extended Data Fig. 7b) plasmids at 37 °C for 15 min in transcription buffer (100 mM Tris-HCl pH 8.0, 500 mM KCl, 100 mM MgCl₂, 1 mM EDTA, 10 mM DTT and 50 µg ml⁻¹ BSA). Next, 2 U of turbo DNase I (Invitrogen) was added to the sample along with turbo DNase I reaction buffer (Invitrogen; final concentration 1×) and incubated at 37 °C for 15 min to fully digest all DNA substrate present in the reaction, effectively halting transcription. DNase I digestion was stopped by adding EDTA to 15 mM (final) and RNA was extracted with the RNA clean and concentrator kit (Zymo Research). Eluted RNA was combined with Qubit high-sensitivity (HS) RNA reagent and Qubit HS RNA buffer and measured using a Qubit fluorometer using the HS RNA protocol after RNA standardization (Life Technologies). The size profile of the RNA sample was analyzed on an Agilent 2200 TapeStation using an HS RNA Screentape with RNA sample buffer (Agilent). The results were visualized using the Agilent TapeStation software (Agilent). For RNase H sensitivity experiments, transcription was halted before the introduction of turbo DNase I by the addition and 5-min incubation of 5 µM rifampicin at 37 °C. Subsequently, 2.5 U of RNase H (New England Biolabs) was added to the reaction and incubated at 37 °C for 5 min.

BCM growth assays. The *rapA* KO strain (F⁻, Δ*hepA769::kan*, Δ(*araD-araB*)567, Δ*lacZ4787::rrnB-3*), λ⁻, *rph-1*, Δ(*rhaD-rhaB*)568, *hsdR514*; Keio collection, National BioResource Project entry JW0058) and wt parental strain (*E. coli* BW25113; National BioResource Project entry ME9062) were both separately transformed with plasmids pBAD18 (empty vector)⁷⁴ or pBAD18*rnhA* (RNase HI)⁵¹ and grown overnight on LB agar plates with 100 µg ml⁻¹ ampicillin. Colonies were picked and grown overnight in LB with 100 µg ml⁻¹ ampicillin and then back diluted to an OD₆₀₀ of 0.01 in LB. L-Arabinose was added to a final concentration of 0.05% (w/v) for induction. Culture solutions (50 µl) were dispensed into dark-well tissue culture plates (Greiner Bio-One CELLSTAR, 384-well) along with BCM (when used, from a 2.5 g L⁻¹ stock in DMSO; Santa Cruz Biotechnology, CAS 38129-37-2) using an HP D300e Digital Dispenser (Tecan). The MIC for BCM was determined to be 37.5 mg L⁻¹.

NaCl growth assays

The *rapA* KO strain and wt parental strain were separately transformed with plasmids pBAD18 (empty vector) and pBAD18*rnhA* and grown overnight on 100 µg ml⁻¹ ampicillin LB agar plates. Colonies were picked and grown overnight in LB with 100 µg ml⁻¹ ampicillin. Culture concentrations were standardized according to OD₆₀₀ measurements and were diluted in a 1:10 dilution series, using LB combined with a final concentration of 0.05% arabinose. Then, 2-µl samples from the 1:10 dilution series of all four culture strains were plated onto separate quadrants of LB agar plates composed of LB agar, 0.9 M NaCl and 0.05% arabinose. Plates were incubated at 37 °C for 48 h and then photographed.

Figures and statistical calculations

Figures and statistical calculations were completed using GraphPad Prism 10.3.1 (Figs. 3b and 4a,b and Extended Data Figs. 6c, 7c and 8), PyMOL 2.5.5 (Figs. 1f,g and 2b–d and Extended Data Figs. 4, 5d and 6a,b) and ChimeraX 1.4 (Figs. 1c–e and 2a and Extended Data Figs. 2b,e,h, 3 and 5c).

Reporting summary

Further information on research design is available in the Nature Portfolio Reporting Summary linked to this article.

Data availability

The cryo-EM density maps and atomic coordinates were deposited to the EM Data Bank (<https://www.ebi.ac.uk/emdb>) and PDB (<https://www.rcsb.org>) as follows: rPTCc (EMD-40930, PDB 8T00), rPTCi (EMD-40931, PDB 8T02), rPTCo (EMD-40922, PDB 8SZW) and RapA¹-PTC (EMD-40943, PDB 8TOL). The atomic models used for initial model building and analysis are available from the PDB under the accession codes 6ALH and 7M8E. Source data are provided with this paper.

References

75. Morin, A. et al. Collaboration gets the most out of software. *eLife* **2**, e01456 (2013).
76. Tetone, L. E. et al. Dynamics of GreB–RNA polymerase interaction allow a proofreading accessory protein to patrol for transcription complexes needing rescue. *Proc. Natl Acad. Sci. USA* **114**, E1081–E1090 (2017).
77. Olinares, P. D. B. et al. A robust workflow for native mass spectrometric analysis of affinity-isolated endogenous protein assemblies. *Anal. Chem.* **88**, 2799–2807 (2016).
78. Olinares, P. D. B. & Chait, B. T. Native mass spectrometry analysis of affinity-captured endogenous yeast RNA exosome complexes. *Methods Mol. Biol.* **2062**, 357–382 (2019).
79. Marty, M. T. et al. Bayesian deconvolution of mass and ion mobility spectra: from binary interactions to polydisperse ensembles. *Anal. Chem.* **87**, 4370–4376 (2015).
80. Reid, D. J. et al. High-throughput deconvolution of native mass spectra. *J. Am. Soc. Mass. Spectrom.* **30**, 118–127 (2019).
81. Chen, J., Noble, A. J., Kang, J. Y. & Darst, S. A. Eliminating effects of particle adsorption to the air/water interface in single-particle cryo-electron microscopy bacterial RNA polymerase and CHAPSO. *J. Struct. Biol.* **X1**, 100005 (2019).
82. Suloway, C. et al. Automated molecular microscopy: the new Leginon system. *J. Struct. Biol.* **151**, 41–60 (2005).
83. Zheng, S. Q. et al. MotionCor2: anisotropic correction of beam-induced motion for improved cryo-electron microscopy. *Nat. Methods* **14**, 331–332 (2017).
84. Punjani, A., Rubinstein, J. L., Fleet, D. J. & Brubaker, M. A.cryoSPARC: algorithms for rapid unsupervised cryo-EM structure determination. *Nat. Methods* **14**, 290–296 (2017).

85. Zivanov, J., Nakane, T. & Scheres, S. H. W. A Bayesian approach to beam-induced motion correction in cryo-EM single-particle analysis. *IUCr* **6**, 5–17 (2018).
86. Tan, Y. Z. et al. Addressing preferred specimen orientation in single-particle cryo-EM through tilting. *Nat. Methods* **14**, 793–796 (2017).
87. Pettersen, E. F. et al. UCSF Chimera—a visualization system for exploratory research and analysis. *J. Comput. Chem.* **25**, 1605–1612 (2004).
88. Afonine, P. V. et al. New tools for the analysis and validation of cryo-EM maps and atomic models. *Acta Crystallogr. D* **74**, 814–840 (2018).
89. Adams, P. D. et al. PHENIX: a comprehensive Python-based system for macromolecular structure solution. *Acta Crystallogr. D* **66**, 213–221 (2010).
90. Emsley, P. & Cowtan, K. Coot: model-building tools for molecular graphics. *Acta Crystallogr. D* **60**, 2126–2132 (2004).

Acknowledgements

We thank C. Gross and members of the S.A.D., E.A.C. and J.G. laboratories for helpful discussions, M. Drolet (University of Montreal) for pBAD18 and pBAD18*rnhA* and M. Ebrahim, J. Sotiris and H. Ng at The Rockefeller University Evelyn Gruss Lipper Cryo-EM Resource Center for help with cryo-EM data collection and analysis. Some of the work reported here was conducted at the Simons EM Center and the National Resource for Automated Molecular Microscopy located at the New York Structural Biology Center, supported by grants from the National Institutes of Health (NIH) National Institute of General Medical Sciences (P41 GM103310), NYSTAR, the Simons Foundation (SF349247), the NIH Common Fund Transformative high-resolution cryo-EM program (U24 GM129539) and NY State Assembly Majority. This work was supported by NIH grants P41 GM109824 and P41 GM103314 to B.T.C., R01 GM38330 to R.L., R01 GM081648 to J.G. and R35 GM118130 to S.A.D.

Author contributions

Conceptualization: J.J.B., K.I., J.G., E.A.C. and S.A.D. Cloning, protein purification and biochemistry: J.J.B., K.I. and R.A.M. MS measurements: P.D.B.O. Cryo-EM specimen preparation, data collection and processing: J.J.B. and L.P.M. Model building and structural analysis: J.J.B., L.P.M., E.A.C. and S.A.D. Single-molecule experiments: K.I. and J.G. Cell growth assays: J.J.B. and B.B. Funding acquisition and supervision: B.T.C., R.L., J.G., E.A.C. and S.A.D. Paper first draft: J.J.B. and S.A.D. All authors contributed to finalizing the written manuscript.

Competing interests

The authors declare no competing interests.

Additional information

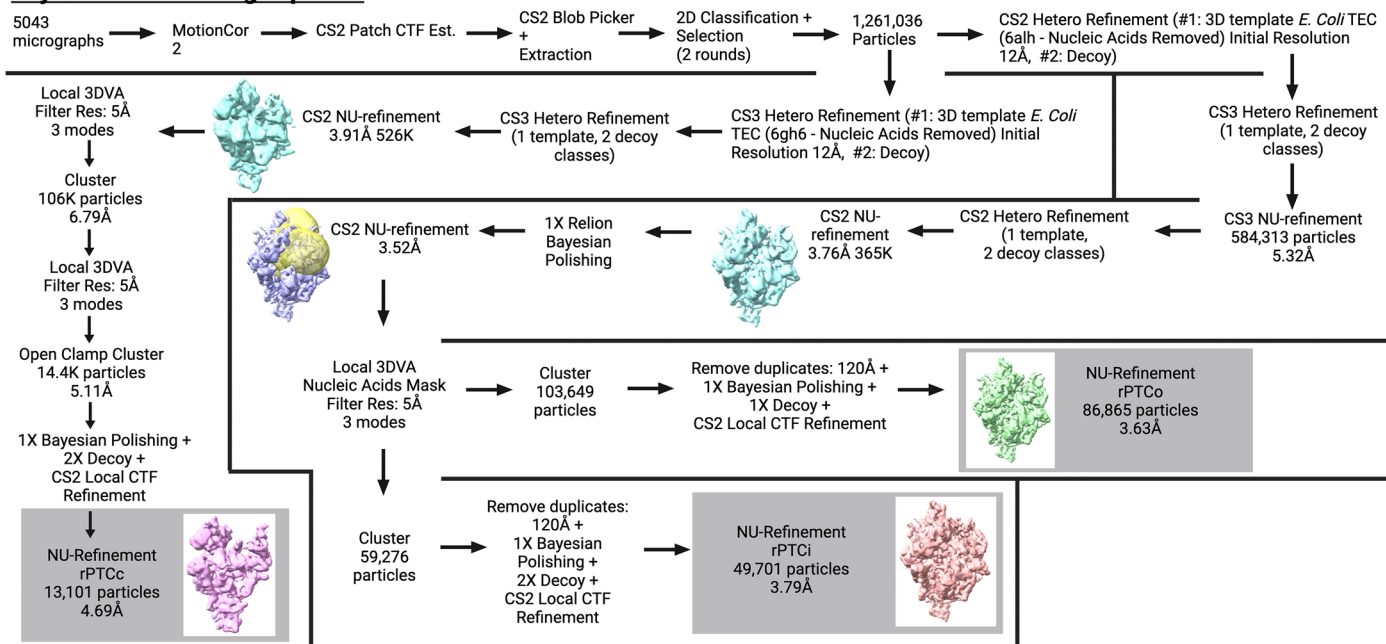
Extended data is available for this paper at <https://doi.org/10.1038/s41594-024-01447-8>.

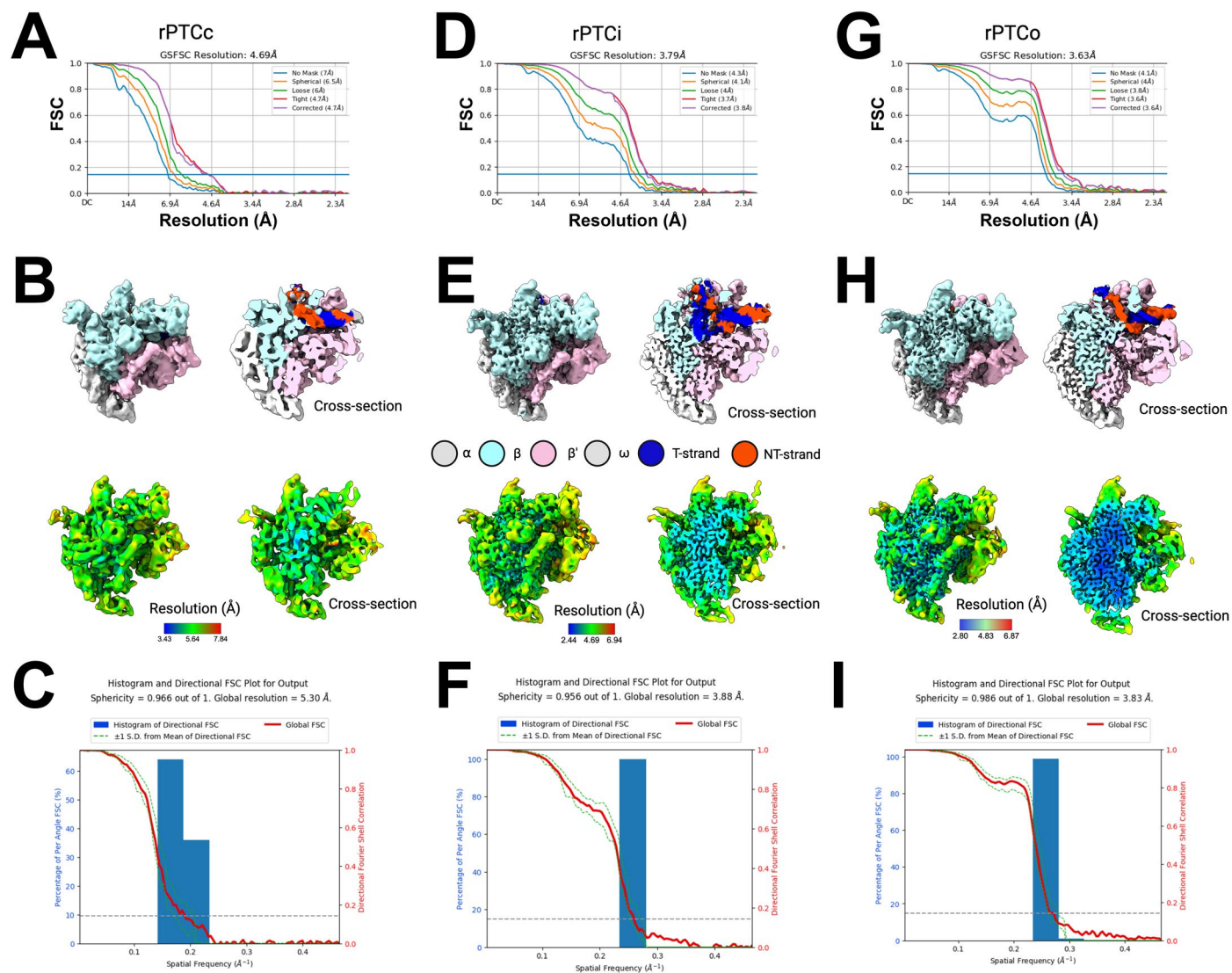
Supplementary information The online version contains supplementary material available at <https://doi.org/10.1038/s41594-024-01447-8>.

Correspondence and requests for materials should be addressed to Seth A. Darst.

Peer review information *Nature Structural & Molecular Biology* thanks the anonymous reviewers for their contribution to the peer review of this work. Primary Handling Editor: Dimitris Typas, in collaboration with the *Nature Structural & Molecular Biology* team.

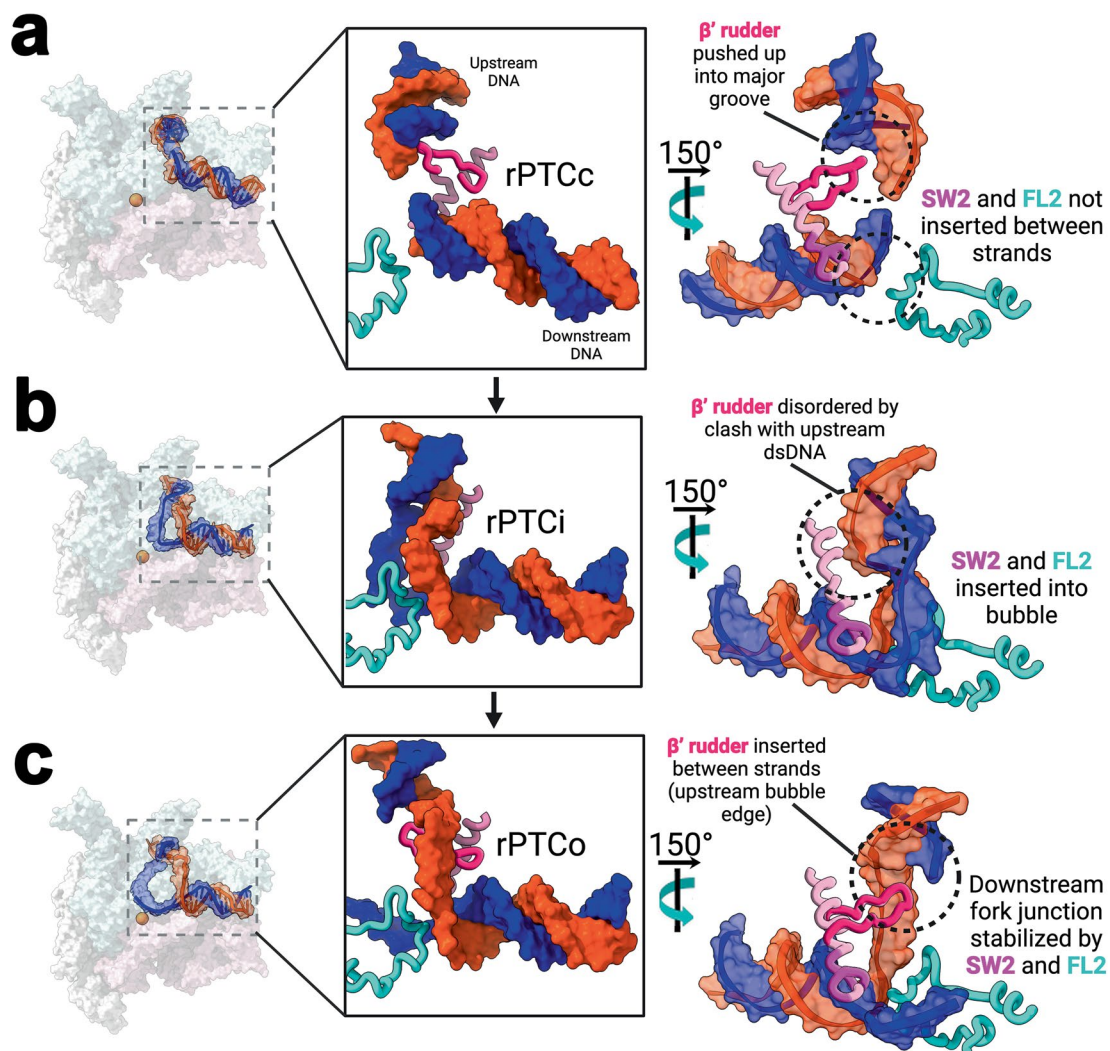
Reprints and permissions information is available at www.nature.com/reprints.

Cryo EM Processing Pipeline**Extended Data Fig. 1 | Cryo-EM processing pipeline for rPTC structures.** Cryo-EM processing pipeline for rPTC structures (rPTCo, rPTCi, rPTCc).



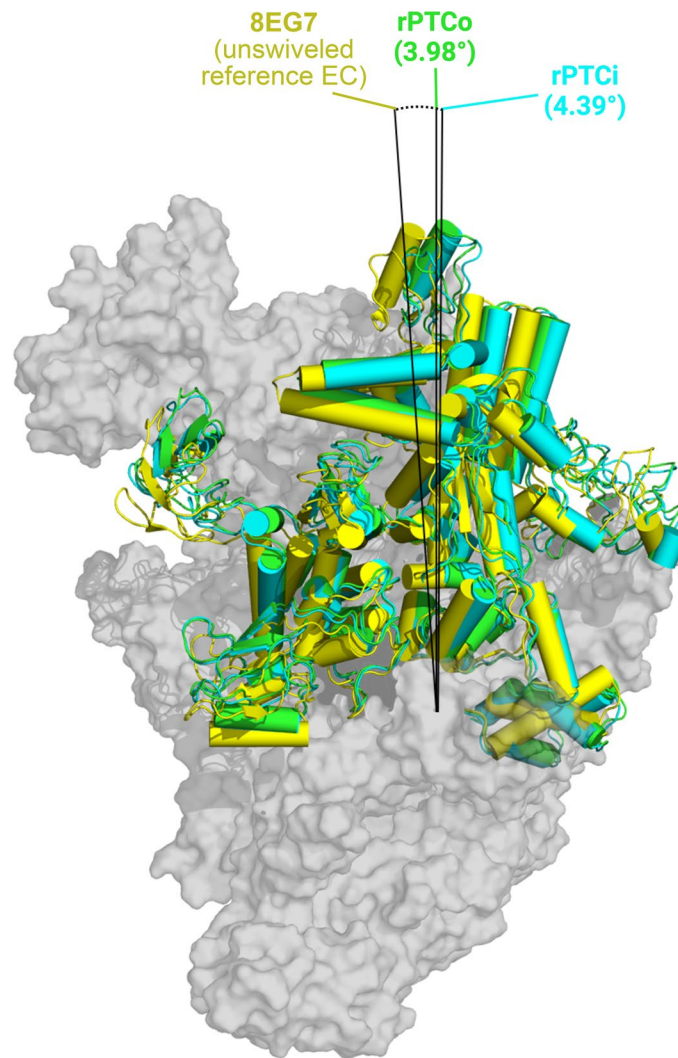
Extended Data Fig. 2 | Cryo-EM of rPTCc, rPTCi, and rPTCo. **a–c.** rPTCc class: Gold standard FSC calculations for cryo-EM density map (A), cryo-EM density map and cross section colored according to key (top of B), cryo-EM density map colored according to local resolution (bottom of B)⁷¹, 3DFSC and sphericity of density map (C)⁸⁴. **d–f.** rPTCi class: Gold standard FSC calculations for cryo-EM density map (D), cryo-EM density map and cross section colored according to key

(top of E), cryo-EM density map colored according to local resolution (bottom of E)⁷¹, 3DFSC and sphericity of density map (F)⁸⁴. **g, h, i.** rPTCo class: Gold standard FSC calculations for cryo-EM density map (G), cryo-EM density map and cross section colored according to key (top of H), cryo-EM density map colored according to local resolution (bottom of H)⁷¹, 3DFSC and sphericity of density map (I)⁸⁴.

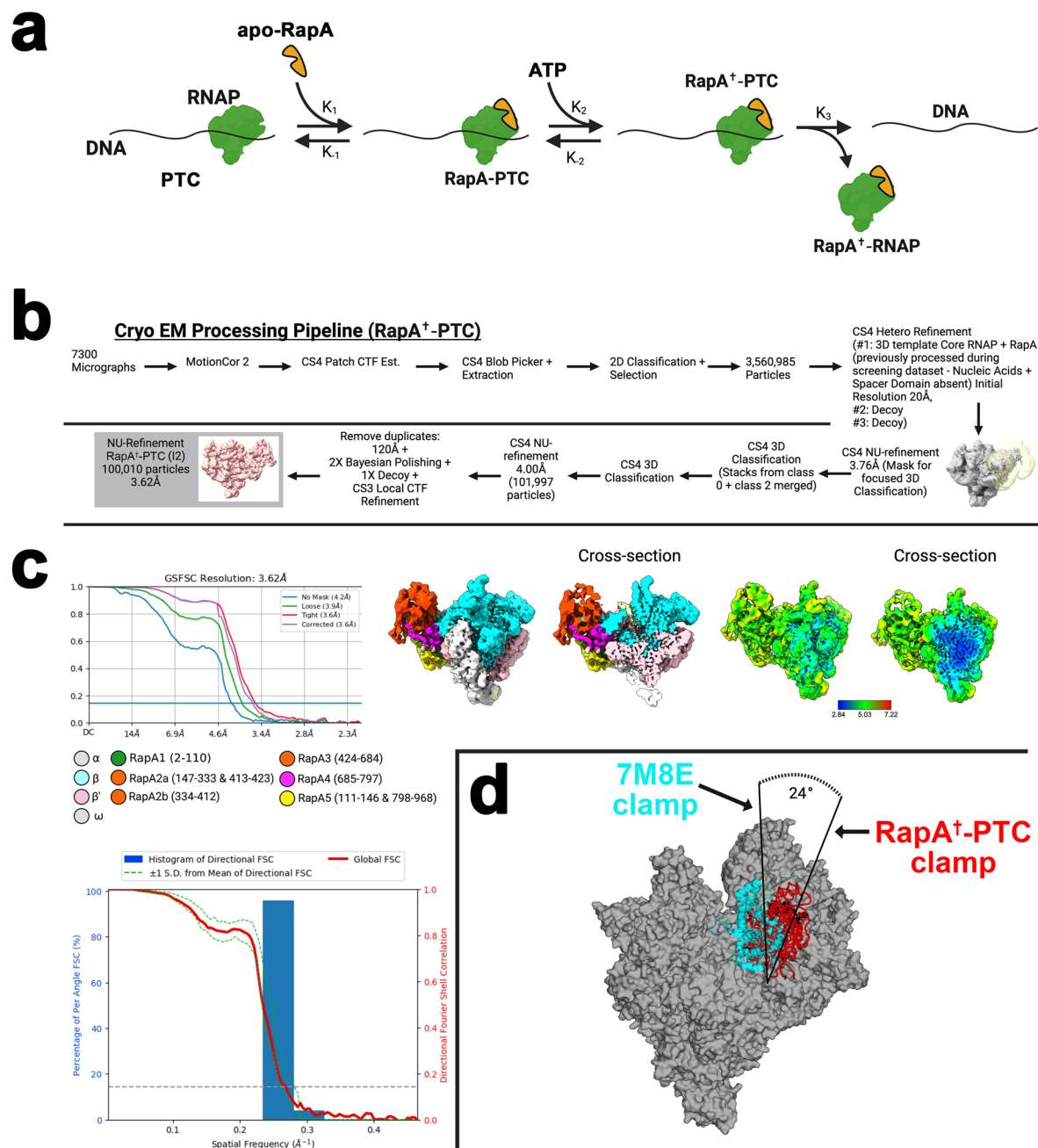


Extended Data Fig. 3 | The role of RNAP structural elements in DNA melting. A.-C. (left) View of the rPTC structures (same as Fig. 1c-e). The boxed regions are magnified on the right. (right) Magnified views of boxed region; only the DNA, β Fork-loop2 (FL2), β' rudder, and β' Switch2 (Sw2) are shown. DNA is shown as a backbone cartoon with a transparent molecular surface (t-strand, blue; nt-strand, orange). The protein elements are shown as backbone cartoons (β , cyan;

β' , pink). **a** rPTCc; the clamp is open 24° , resulting in a large separation between FL2 and Sw2. **b**. rPTCi; the clamp closes, closing the gap between FL2 and Sw2, nucleating a - 5 nt bubble in the DNA. The β' rudder is completely disordered. **c**. rPTCo; the bubble propagates in the upstream direction to -7-8 nt, creating room for the β' rudder.

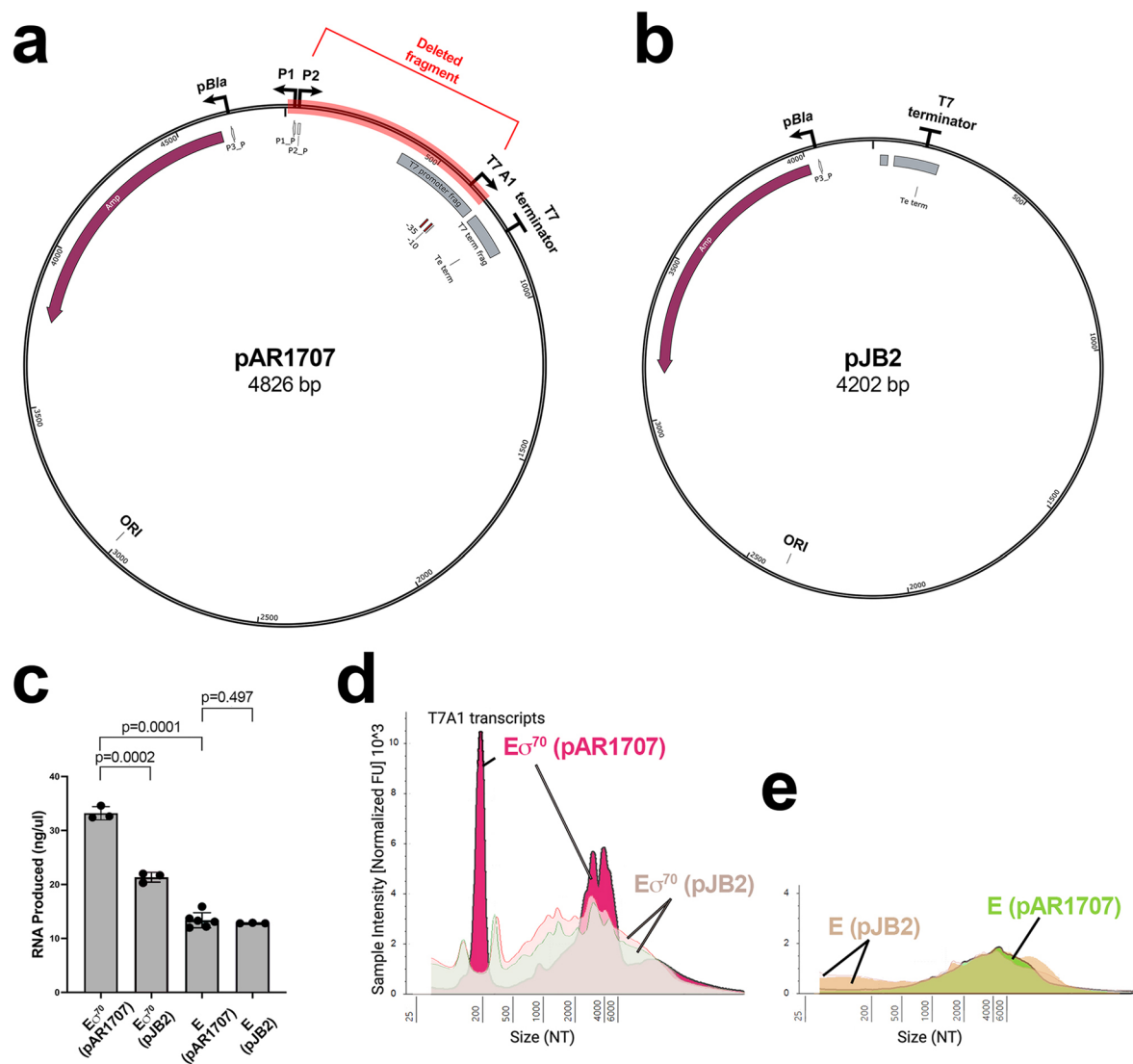


Extended Data Fig. 4 | Swiveling in rPTCi and rPTCo. RNAP structures are shown as a gray molecular surface but with the swivel modules³⁸ shown as backbone cartoons with cylindrical helices [8EG7³⁸ (unswiveled reference EC), yellow; rPTCo, green; rPTCi, cyan]. Rotation (swiveling) of the rPTCo and rPTCi swivel modules with respect to 8EG7 is shown.



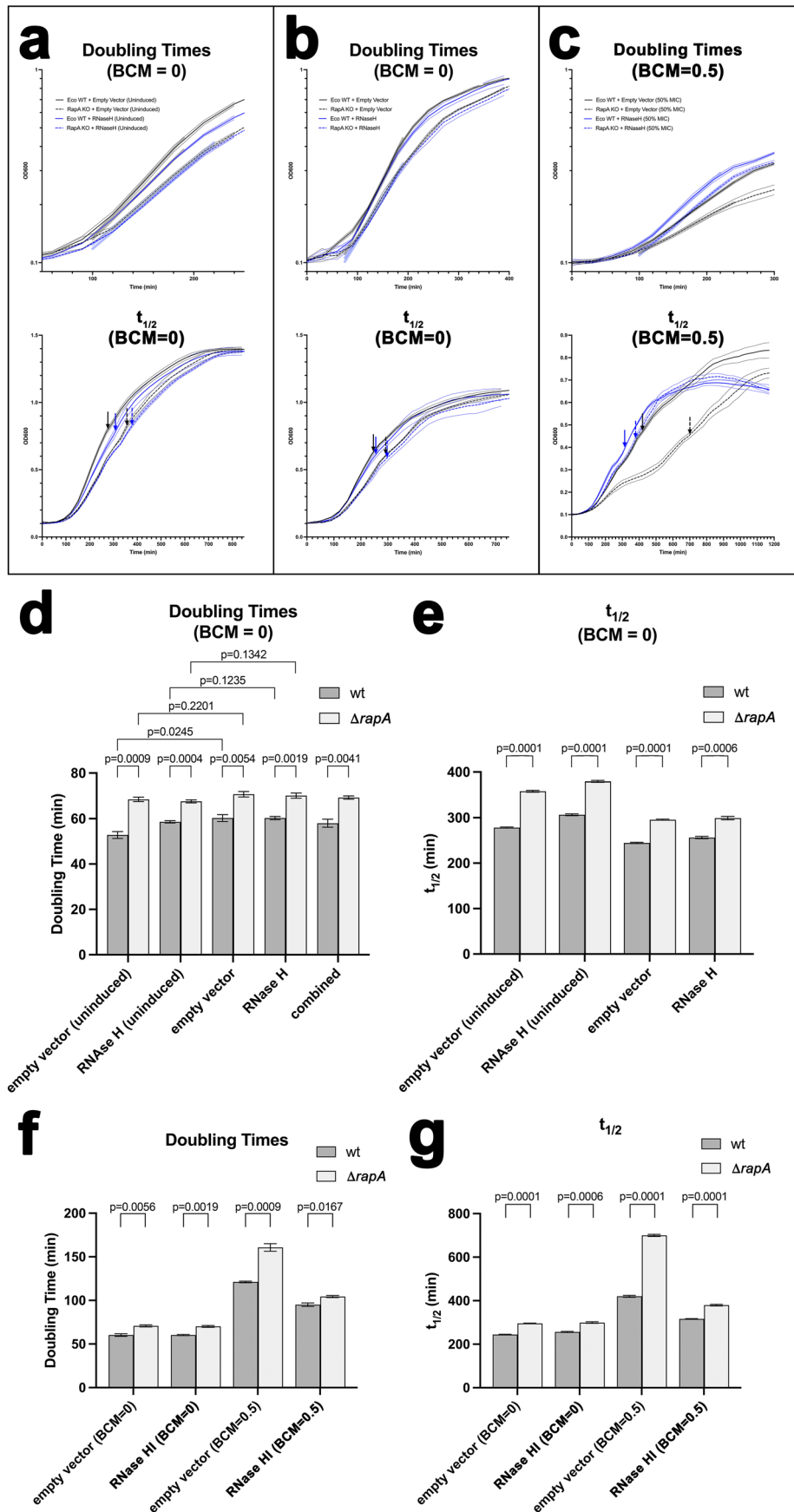
Extended Data Fig. 5 | RapA⁺-PTC. **a.** Hypothesized mechanism for the disruption of the PTC by RapA, adapted from⁷. **b.** Cryo-EM processing pipeline for RapA⁺-PTC class. **c.** Gold standard FSC calculations for the cryo-EM density map (upper left), cryo-EM density map and cross section colored according to key (upper middle), cryo-EM density map colored according to local resolution

(upper right)⁷¹, 3DFSC and sphericity of density map (lower)⁸⁴. **d.** Range of RNAP clamp movement observed in the transition between RapA-PTC stand-in (PDB: 7M8E) and observed RapA⁺-PTC. Clamp opens approximately 24° upon RapA-PTC conformation change driven by ATP binding.



Extended Data Fig. 7 | *In vitro* transcription reactions on pJB2. a. Plasmid map showing relevant features of pAR1707 (including annotated promoters). The region deleted to generate pJB2 is highlighted in red. **b.** Plasmid map showing relevant features of pJB2. **c.** Histogram plot showing the total amount of RNA produced from transcription reactions. The bars denote the average of three to six independent measurements (individual data points shown). Data are presented as mean values \pm SEM. Statistical significance of differences between

samples was determined using an unpaired, two-tailed *t*-test. **d.** Size distribution of transcripts resulting from two independent E σ^{70} transcription reactions using pJB2 as a template (light shades) compared with the original size distribution of transcripts resulting from E σ^{70} transcription from pAR1707 (hot pink, see Fig. 3c). **e.** Size distribution of transcripts resulting from core RNAP (E) reactions using pJB2 as a template (light shades) compared with the original size distribution of transcripts resulting from E transcription from pAR1707 (see Fig. 3d).



Extended Data Fig. 8 | See next page for caption.

Extended Data Fig. 8 | Growth analysis of wt and $\Delta rapA$ Eco. a–c. Growth curves ($OD_{600\text{nm}}$). The solid lines plot the average of three replicates, the thin lines above and below show the 95% confidence limit. (*top panel*) Semi-log plots of the growth curves during log-phase growth. The thick, transparent lines show the exponential fit used to calculate the doubling time. (*bottom panel*) Linear scale showing the full growth curves. The thick arrows denote the $t_{1/2}$. **a.** BCM = 0 and in the absence of arabinose [uninduced pBAD18 (empty vector) or pBAD18*rnhA* (RNase H)]. **b.** BCM = 0 but with arabinose induction (0.05% w/v) of pBAD18 (empty vector) or pBAD18*rnhA* (RNase H). **c.** BCM = 0.5X MIC (MIC = 37.5 mg/L) and with arabinose induction (0.05% w/v) of pBAD18 (empty vector) or pBAD18*rnhA* (RNase H). **d.–e.** Histograms showing growth parameters [double times (d) and $t_{1/2}$ (e)] for wt and $\Delta rapA$ Eco cells carrying pBAD18 (empty vector)⁷⁴ or pBAD18*rnhA* (RNase H)⁵¹, all without BCM (BCM = 0). In d., combined is the average for all the measurements. Error bars denote standard error (N = 3 independent growth curves for each condition). Statistical significance of

differences between samples was determined using unpaired, two-tailed *t*-test. **d.** Doubling times (N = 3 independent growth curves for each condition). Data are presented as best fit values \pm SEM (calculated from 95% confidence limits of best fit). **e.** $t_{1/2}$ (N = 3 independent growth curves for each condition). Data are presented as best fit values \pm SEM (calculated from 95% confidence limits of best fit). **f.–g.** Histograms showing growth parameters (doubling times and $t_{1/2}$) for wt and $\Delta rapA$ Eco cells carrying pBAD18 (empty vector)⁷⁴ or pBAD18*rnhA* (RNase H)⁵¹ without (BCM = 0) or with 0.5X MIC BCM (BCM = 0.5). Error bars denote standard error (N = 3 independent growth curves for each condition). Statistical significance of differences between samples was determined using an unpaired, two-tailed *t*-tests. **f.** Doubling times (N = 3 independent growth curves for each condition). Data are presented as best fit values \pm SEM (calculated from 95% confidence limits of best fit). **g.** $t_{1/2}$ (N = 3 independent growth curves for each condition). Data are presented as best fit values \pm SEM (calculated from 95% confidence limits of best fit).

Reporting Summary

Nature Portfolio wishes to improve the reproducibility of the work that we publish. This form provides structure for consistency and transparency in reporting. For further information on Nature Portfolio policies, see our [Editorial Policies](#) and the [Editorial Policy Checklist](#).

Statistics

For all statistical analyses, confirm that the following items are present in the figure legend, table legend, main text, or Methods section.

- | n/a | Confirmed |
|-------------------------------------|--|
| <input type="checkbox"/> | <input checked="" type="checkbox"/> The exact sample size (n) for each experimental group/condition, given as a discrete number and unit of measurement |
| <input checked="" type="checkbox"/> | <input type="checkbox"/> A statement on whether measurements were taken from distinct samples or whether the same sample was measured repeatedly |
| <input type="checkbox"/> | <input checked="" type="checkbox"/> The statistical test(s) used AND whether they are one- or two-sided
<i>Only common tests should be described solely by name; describe more complex techniques in the Methods section.</i> |
| <input checked="" type="checkbox"/> | <input type="checkbox"/> A description of all covariates tested |
| <input checked="" type="checkbox"/> | <input type="checkbox"/> A description of any assumptions or corrections, such as tests of normality and adjustment for multiple comparisons |
| <input type="checkbox"/> | <input checked="" type="checkbox"/> A full description of the statistical parameters including central tendency (e.g. means) or other basic estimates (e.g. regression coefficient) AND variation (e.g. standard deviation) or associated estimates of uncertainty (e.g. confidence intervals) |
| <input checked="" type="checkbox"/> | <input type="checkbox"/> For null hypothesis testing, the test statistic (e.g. F , t , r) with confidence intervals, effect sizes, degrees of freedom and P value noted
<i>Give P values as exact values whenever suitable.</i> |
| <input checked="" type="checkbox"/> | <input type="checkbox"/> For Bayesian analysis, information on the choice of priors and Markov chain Monte Carlo settings |
| <input checked="" type="checkbox"/> | <input type="checkbox"/> For hierarchical and complex designs, identification of the appropriate level for tests and full reporting of outcomes |
| <input checked="" type="checkbox"/> | <input type="checkbox"/> Estimates of effect sizes (e.g. Cohen's d , Pearson's r), indicating how they were calculated |

Our web collection on [statistics for biologists](#) contains articles on many of the points above.

Software and code

Policy information about [availability of computer code](#)

Data collection	<input type="text" value="Leginon 3.6"/>
Data analysis	<input type="text" value="Structural biology software was accessed through the SBGrid consortium (ref. 72). MotionCor2 1.6.4."/> <input type="text" value="CryoSPARC v3.1.0 (ref. 80)"/> <input type="text" value="RELION 3.1 (ref. 81)"/> <input type="text" value="Bsoft package 2.1.3 (ref. 71)"/> <input type="text" value="3DFSC package 3.0 (ref. 82) ChimeraX 1.4 (ref. 83)"/> <input type="text" value="Phenix 1.21-5207 (ref. 84,85)"/> <input type="text" value="COOT 0.9.8.92 (ref. 86)"/> <input type="text" value="Thermo Xcalibur Qual Browser v.4.2.47 UniDec v.4.2.0 (ref. 75, 76)"/> <input type="text" value="PyMOL v2.5.5"/> <input type="text" value="GraphPad Prism 10.3.1"/>

For manuscripts utilizing custom algorithms or software that are central to the research but not yet described in published literature, software must be made available to editors and reviewers. We strongly encourage code deposition in a community repository (e.g. GitHub). See the Nature Portfolio [guidelines for submitting code & software](#) for further information.

Data

Policy information about [availability of data](#)

All manuscripts must include a [data availability statement](#). This statement should provide the following information, where applicable:

- Accession codes, unique identifiers, or web links for publicly available datasets
- A description of any restrictions on data availability
- For clinical datasets or third party data, please ensure that the statement adheres to our [policy](#)

Data availability. The cryo-EM density maps and atomic coordinates have been deposited in the EMDDataBank (<https://www.ebi.ac.uk/emdb>) and Protein Data Bank (<https://www.rcsb.org>) as follows: rPTCc (EMD-40930, PDB 8T00), rPTCi (EMD-40931, PDB 8T02), rPTCo (EMD-40922, PDB 8SZW), RapA⁺-PTC (EMD-40943, PDB 80TL). The atomic models used for initial model building and analysis are available from the Protein Data Bank under the accession codes 6ALH, and 7M8E.

Research involving human participants, their data, or biological material

Policy information about studies with [human participants or human data](#). See also policy information about [sex, gender \(identity/presentation\), and sexual orientation](#) and [race, ethnicity and racism](#).

Reporting on sex and gender	<input type="text" value="No research involving human participants is reported"/>
Reporting on race, ethnicity, or other socially relevant groupings	<input type="text" value="No research involving human participants is reported"/>
Population characteristics	<input type="text" value="No research involving human participants is reported"/>
Recruitment	<input type="text" value="No research involving human participants is reported"/>
Ethics oversight	<input type="text" value="No research involving human participants is reported"/>

Note that full information on the approval of the study protocol must also be provided in the manuscript.

Field-specific reporting

Please select the one below that is the best fit for your research. If you are not sure, read the appropriate sections before making your selection.

Life sciences Behavioural & social sciences Ecological, evolutionary & environmental sciences

For a reference copy of the document with all sections, see [nature.com/documents/nr-reporting-summary-flat.pdf](https://www.nature.com/documents/nr-reporting-summary-flat.pdf)

Life sciences study design

All studies must disclose on these points even when the disclosure is negative.

Sample size	The cryo-EM data collections resulted in 1,261,036 (rPTC) and 3,560,985 (RapA ⁺ -PTC) particle images used for subsequent processing (see Extended Data Figures 1 and 5b). For biochemical experiments (Figures 2e, 3, 4, and, Extended Data Figure 6c), 7c, 8, sample size calculations were not performed. In general, experiments were replicated a minimum of three times.
Data exclusions	Particle images were excluded according to criteria encoded in cryoSPARC and Relion.
Replication	The cryo-EM experiments were not replicated. The biochemical experiments were replicated a minimum of three times (Figs. 3b, 4, and Extended Data Figs. 7c-e, 8) or hundreds of times (Fig. 2e, Extended Data Fig. 6c)
Randomization	The structural analysis was not randomized. Control of covariates is not applicable as all known parameters were controlled.
Blinding	In the structural analysis, the classification of particles into structural classes was blinded to investigators.

Reporting for specific materials, systems and methods

We require information from authors about some types of materials, experimental systems and methods used in many studies. Here, indicate whether each material, system or method listed is relevant to your study. If you are not sure if a list item applies to your research, read the appropriate section before selecting a response.

Materials & experimental systems

n/a	Involvement in the study
<input checked="" type="checkbox"/>	<input type="checkbox"/> Antibodies
<input checked="" type="checkbox"/>	<input type="checkbox"/> Eukaryotic cell lines
<input checked="" type="checkbox"/>	<input type="checkbox"/> Palaeontology and archaeology
<input checked="" type="checkbox"/>	<input type="checkbox"/> Animals and other organisms
<input checked="" type="checkbox"/>	<input type="checkbox"/> Clinical data
<input checked="" type="checkbox"/>	<input type="checkbox"/> Dual use research of concern
<input checked="" type="checkbox"/>	<input type="checkbox"/> Plants

Methods

n/a	Involvement in the study
<input checked="" type="checkbox"/>	<input type="checkbox"/> ChIP-seq
<input checked="" type="checkbox"/>	<input type="checkbox"/> Flow cytometry
<input checked="" type="checkbox"/>	<input type="checkbox"/> MRI-based neuroimaging